Algorithmic aspects of the LES-PBE-PDF method for modelling soot particle size distributions in turbulent flames

Fabian Sewerin*

Institute of Solid Mechanics, Technische Universität Braunschweig, Langer Kamp 8, 38106 Braunschweig, Germany

Stelios Rigopoulos

Department of Mechanical Engineering, Imperial College London, Exhibition Road, London SW7 2AZ, UK

Abstract

In recent times, the LES-PBE-PDF framework has been developed to couple large eddy simulation (LES) and population balance models (PBE) for the description of soot formation in turbulent hydrocarbon flames. This approach is based on a modelled evolution equation for the LES-filtered probability density function (*pdf*) associated with the instantaneous gas composition and soot particle size distribution. Here, the interaction of turbulence with chemical reactions and soot formation can be represented without approximations on part of the chemical and soot formation kinetics, while effects due to turbulent transport and molecular diffusion require closure. In view of an efficient numerical solution scheme, we previously proposed to combine a statistically equivalent reformulation of the joint scalar-number density *pdf* based on Eulerian stochastic fields with a time-explicit adaptive grid discretization in particle size space and a fractional time stepping scheme.

In this article, we present algorithmic aspects and relay implementational details for a consistent semi-discrete formulation of the PBE fractional step as well as an effective dynamic load balancing scheme for both the chemical reaction and PBE fractional steps. Considering soot formation in the Delft III turbulent diffusion flame as a test case, we show that the persisting load imbalance is almost negligible on average and give evidence of linear strong scaling on a modern high performance computer for moderate numbers of compute nodes.

Keywords: LES-PDF method, Population balance, Stochastic fields, Grid adaptivity, Dynamic load balancing

1 Introduction

The emission of soot from hydrocarbon flames continues to remain a major concern. Soot constitutes a particulate phase that is created from an ambient gas phase and interacts with precursor species as particles grow, mature, aggregate and, possibly, oxidize. If the carrier flow is turbulent, then both chemical reactions in the gas phase and soot formation processes can be strongly modulated by the velocity fluctuations in the carrier flow. Since soot particles are polydisperse, for example, with respect to a representative measure of size, they are commonly characterized by a particle size distribution. The particle size distribution naturally mediates between a Lagrangian viewpoint in which particles are tracked individually and a Eulerian perspective and may be instrumented to transition from a particle based physical model to the so-called population balance equation (PBE) [13]. Formally, the PBE represents an evolution equation for the distribution of particle number density over both physical and particle size space.

In recent years, researchers have investigated incorporating the PBE into Reynolds averaged (RANS) and large eddy simulation (LES) frameworks for the representation of turbulence effects with an objective to predict soot particle size distributions at high Reynolds numbers. The closure problems that occur here are very similar to the ones encountered in chemically reacting gaseous flows, for example, combustion, and, physically, reflect the interaction of turbulence, chemical reactions and particle formation [5, 43, 44]. In the absence of soot formation, the turbulence-chemistry interaction is often resolved with the aid of PDF methods which are based on the joint probability density function (*pdf*)[1] associated with the gas phase composition at a particular spatial location and point in time. This joint scalar *pdf* can either

*Corresponding author (f.sewerin@tu-braunschweig.de)

[1] By convention, we use uppercase letters (PDF) to refer to PDF approaches in general and italic lowercase letters (*pdf*) when discussing *a* particular probability density function.

be reconstructed from modelled evolution equations for its low order statistics (presumed *pdf* methods) or may be obtained from a modelled evolution equation (transported *pdf* methods [14]). An important characteristic of the second class of approaches is that the reaction source terms can be resolved without approximation, while spatial two-point correlations and velocity-scalar statistics require closure.

Just about a decade ago, Rigopoulos [43] showed that the unclosed scalar-number density correlations that occur in RANS reformulations of the PBE may be circumvented by incorporating the number density in the transported PDF formalism. He argued that, upon discretization along the particle size coordinate, the PBE reduces to a number of evolution equations for discrete number densities which are, conceptually, akin to the reactive scalar transport equations that characterize the gas phase. By this rationale and with the aid of established techniques [23, 35], an evolution equation for the joint scalar-discrete number density *pdf* was obtained. The main advantage of this PBE-PDF approach is that the Reynolds averaged fluid composition and particle size distribution can be resolved without any approximation on part of the chemical reaction mechanism or particle formation kinetics. For spatially inhomogeneous turbulent flows, the RANS-PBE-PDF equation seems to have first been deployed by Di Veroli and Rigopoulos [5, 6, 7] who investigated crystal precipitation in a coaxial pipe mixer and droplet condensation in a turbulent round jet. While the particle-laden flows in these applications were incompressible with a constant density, the PBE-PDF framework may similarly be formulated for the variable density flows we encounter in combustion. Akridis and Rigopoulos [2] and Akridis [1], for example, showed how the RANS-PBE-PDF methodology can be adopted for the prediction of soot particle size distributions in turbulent diffusion flames due to nucleation and growth/oxidation. Very recently, this approach was also adopted by Schiener and Lindstedt [49] who incorporated soot particle coagulation and employed acetylene-based nucleation/growth kinetics that were calibrated based on a comprehensive chemical reaction mechanism and pyrene-based soot inception kinetics [48].

Conceptually, the PDF closures that were originally developed in the context of RANS can similarly be developed for LES [9, 36]; here, the scalar one-point, one-time statistics rely on the LES-filtered *pdf* associated with a single realization of the governing fields. Strictly, this *pdf* continues to remain a random variable [32], but statistic consistency can be restored by conditioning on (a discrete representation of) a particular LES-filtered realization [8, 37]. Although self-conditioning has important implications for the physical rationalization of turbulent transport and micromixing closures, the PDF formalism may be developed in a similar way for both the LES-filtered instantaneous *pdf* (which we consider in this article) and the self-conditioned *pdf* [37, Appendix C]. For applications involving aerosol nucleation and growth, the PBE-PDF approach appears to have first been incorporated into LES by Neuber et al. [28] and Sewerin and Rigopoulos [51], albeit in slightly different ways. While Neuber et al. [28] based their developments on a joint scalar-discrete number density *pdf*, Sewerin and Rigopoulos [51] found that the PBE-PDF framework may also be developed independent of a particular *a priori* discretization of the PBE in particle size space. This line of thought led to a transport equation for the joint scalar-number density *pdf* which, upon reformulation in terms of statistically equivalent stochastic differential equations (SDEs), allowed for the application of different fixed or adaptive grid discretization schemes in particle size space. Shortly afterwards, the LES-PBE-PDF framework was generalized to combusting flows at low Mach numbers by Sewerin and Rigopoulos [52] and applied to the prediction of soot particle size distributions in a turbulent diffusion flame. Concurrently, Neuber et al. [27] applied an LES-PBE-PDF formulation to the synthesis of silica particles in a turbulent jet flow configuration, comparing predictions of laser diagnostic signals with measurements.

Many of the PBE-PDF references mentioned above invoked a stochastic particle-based scheme [12, 35] in order to approximate and evolve statistics of the joint scalar-discrete number density *pdf*. Recently, Neuber et al. [28] showed that a sparse particle variant of these schemes may be constructed in the context of LES by combining a micromixing model with generalized multiple mapping conditioning (MMC) [56]. The main idea was to deemphasize physical proximity of stochastic particles which are selected for micromixing, while ensuring locality of the mixing operation in mixture fraction space. A very positive consequence was that the overall computational expense could be reduced by about one order of magnitude. Despite the dominance of stochastic particle methods, an alternative approach that has recently attracted more attention and mainly emerged for LES of gas phase combustion [16] is the method of Eulerian stochastic fields [46, 55]. Here, the statistical sampling error is spatially uniform and the governing space-dependent SDEs are amenable to incorporation into existing Eulerian flow solvers. In the context of the LES-PBE-PDF method, Sewerin and Rigopoulos [51, 52] reformulated the joint scalar-number density *pdf* equation in terms of statistically equivalent Eulerian stochastic fields. They further demonstrated that the computational expense stemming from the numerical solution of the stochastic field

Variable/Operator	Explanation
n_s	Number of gas phase scalars
n_f	Number of stochastic fields
n_p	Number of finite volume cells in τ-space, $[l_l, L]$
n_c	Number of spatial finite volume cells
n_{mpi}	Number of MPI processes
n_d	Number of parcels dispatched/sent by MPI process id
n_r	Number of parcels received by MPI process id
$\bar{\cdot}$	LES-filter/Expectation with respect to $f(\mathbf{y}, n(\cdot); \mathbf{x}, t)$
$\tilde{\cdot}$	Favre-filter/Expectation with respect to $\tilde{f}(\mathbf{y}, n(\cdot); \mathbf{x}, t)$
$\langle\cdot\rangle_{n_f}$	Monte Carlo estimate based on n_f stochastic fields
$\langle\cdot\rangle_{\Omega_j}$	Spatial average on Ω_j

Table 1: Summary of the important number variables and operators that are employed in this article.

equation for the PBE can be significantly reduced with the aid of an explicit adaptive grid discretization scheme in particle size space [50].

While our focus lies on the treatment of population balance models within the scope of LES-transported *pdf* methods, we mention that presumed *pdf* approaches for LES have been developed concurrently [26, 34] and were, recently, also extended to the prediction of soot particle size distributions [45]. Here, the gas phase composition is commonly expressed in terms of a small number of tracking scalars [31], for example, the mixture fraction or a reaction progress variable, and the joint *pdf* of the tracking scalars and the scalars parameterizing the particle size distribution (moments [26] or discrete number densities [45]) is assumed to conform to a prescribed functional form. Mueller and Pitsch [25] argued that soot evolves on much larger time scales than the gas phase composition and, hence, suggested to model the tracking scalars as random fields that are independent of the soot describing scalars. The resulting marginal *pdfs* are typically parameterized by a few low order statistics such as the mixture fraction mean and variance or the mean discrete number densities which can be obtained from modelled evolution equations. The main advantages of presumed *pdf* formulations are linked to their computational economy as only a small number of scalar statistics are transported. Within the course of the past few years, this has allowed researchers to incorporate sophisticated chemical and soot formation kinetics, accounting, for example, for the action of polycyclic aromatic hydrocarbons. On the other hand, we mention that presumed *pdf* methods involve several levels of physical approximation and that the scheme for relating the gas phase composition to tracking scalars often relies on a particular flame structure [42].

In this article, we reconsider the LES-PBE-PDF methodology of Sewerin and Rigopoulos [52] and present the pertinent algorithmic aspects along with implementational details. Our intention is to render the LES-PBE-PDF approach combined with a stochastic field solution scheme, a fractional time stepping and PBE-grid adaptivity more transparent and accessible. To this end, we first discuss in detail the finite volume discretization of the resulting PBE fractional step. Second, a dynamic load balancing scheme is presented and its efficacy and performance for both the reaction and PBE fractional steps are quantified on a modern high performance computing system.

This article is organized as follows: First, the equations governing the evolution of the gas and particulate phases in low Mach number, variable density flows are summarized and the LES-PBE-PDF modelling framework is briefly revisited. Subsequently, we summarize a statistically equivalent stochastic field reformulation with an emphasis on the incorporation of resolution adaptivity in particle size space and the separation of physical processes into distinct fractional steps. In the following section, the finite volume based semi-discrete formulation of the PBE fractional step is presented in detail. This links in with the penultimate section, where we introduce and quantitatively assess a dynamic load balancing scheme for the reaction and PBE fractional steps. Finally, we conclude with a brief summary.

As reference, Table 1 summarizes the important number variables and operators we employ throughout this article.

2 LES-PBE-PDF framework

In this section, we succinctly review the equations governing the evolution of a turbulent reacting flow at low Mach number in which a polydisperse particulate phase is immersed and summarize key aspects of the LES-PBE-PDF formulation. The flow domain is denoted by $\Omega \subseteq \mathbb{R}^3$ and we employ Cartesian coordinates $\mathbf{x} = (x_1, x_2, x_3)$ throughout. In the presence of chemical reactions, the fluid phase is commonly characterized in terms of reactive scalars $\mathbf{Y} = (Y_1, \ldots, Y_{n_s})$, for example, species mass fractions and enthalpy, obeying the transport equations

$$\frac{\partial \rho Y_i}{\partial t} + \sum_{j=1}^{3} \frac{\partial \rho u_j Y_i}{\partial x_j} = -\sum_{j=1}^{3} \frac{\partial J_{ij}}{\partial x_j} + \rho \dot{\omega}_i(\mathbf{Y}, N), \quad i = 1, \ldots, n_s, \tag{1}$$

where $\rho(\mathbf{x}, t)$ denotes the mixture density, $\mathbf{u}(\mathbf{x}, t)$ is the velocity field of the carrier flow and $\dot{\omega}_i(\mathbf{Y}(\mathbf{x}, t), N(\cdot, \mathbf{x}, t))$ represents the kinetic rate of change of scalar i due to chemical reactions, radiation or particle formation. For simplicity and as our focus lies on high Reynolds number flows, the diffusion flux $J_{ij}(\mathbf{Y}(\mathbf{x}, t))$ of scalar i along the jth coordinate direction is expressed in terms of a unique scalar diffusivity $D(\mathbf{x}, t)$,

$$J_{ij}(\mathbf{x}, t) = -\rho(\mathbf{x}, t) D(\mathbf{x}, t) \frac{\partial Y_i(\mathbf{x}, t)}{\partial x_j}. \tag{2}$$

If we consider, at a specific instant in time $t \geq 0$, a group of particles immersed in the flow, then these may be described in terms of their current locations $\mathbf{x} \in \Omega$ as well as a particle property $l \in [l_l, L]$, for example, a measure of size. All remaining properties such as the particle temperature or its velocity are inherited from the ambient fluid or the carrier flow. This reflects the rationale that soot particles are very small, exhibiting a short momentum response time and a Stokes number much less than unity (non-inertial particles) [44]. Adopting a Eulerian perspective, the particulate phase may then be described in terms of the distribution of particles both in physical space and in particle property space. Following Hulburt and Katz [13], this leads to the concept of a particle number density $N(l, \mathbf{x}, t)$; if l indicates particle size, then $N(\cdot, \mathbf{x}, t)$ is often referred to as the particle size distribution. Starting from the Lagrangian equations of motion of a single particle (possibly augmented by effects of Brownian motion), it is possible to show that $N(l, \mathbf{x}, t)$ evolves according to the population balance equation (PBE)

$$\frac{\partial N}{\partial t} + \sum_{j=1}^{3} \frac{\partial u_j N}{\partial x_j} + \frac{\partial G(l, \mathbf{Y}) N}{\partial l} = -\sum_{j=1}^{3} \frac{\partial K_j}{\partial x_j} + \dot{s}(l, \mathbf{Y}, N). \tag{3}$$

Here, $G(l, \mathbf{Y})$ and $\dot{s}(l, \mathbf{Y}(\mathbf{x}, t), N(\cdot, \mathbf{x}, t))$ represent the kinetic rates for particle growth and particle creation/deletion, respectively, and $K_j(l, \mathbf{x}, t)$ denotes the diffusion flux of number density along the jth coordinate direction,

$$K_j(l, \mathbf{x}, t) = -D_p(\mathbf{x}, t) \frac{\partial N(l, \mathbf{x}, t)}{\partial x_j}. \tag{4}$$

For soot particles in turbulent flames, it has been argued that diffusive transport is almost negligible as compared to convective transport [4, 22, 33] and, in line with these arguments, we take the particle diffusion coefficient as $D_p = 0$ identically.

If the fluid phase corresponds to a multicomponent ideal gas and the Mach number is low, then both the mixture temperature $T(\mathbf{x}, t)$ and density $\rho(\mathbf{x}, t)$ can be expressed in terms of the reactive scalars $\mathbf{Y}(\mathbf{x}, t)$ and an ambient reference pressure $p_0(t)$ such that [12, Section 3.6]

$$T(\mathbf{x}, t) = \hat{T}(\mathbf{Y}(\mathbf{x}, t)), \tag{5}$$

$$\rho(\mathbf{x}, t) = \hat{\rho}(\mathbf{Y}(\mathbf{x}, t), p_0(t)). \tag{6}$$

In turbulent jet flow configurations such as the Delft III flame considered below, the reference pressure remains constant in time, $p_0(t) = p_0$. To slightly abridge subsequent expressions, we therefore omit the explicit pressure dependence in Eq. (6), taking $\rho(\mathbf{x}, t) = \hat{\rho}(\mathbf{Y}(\mathbf{x}, t))$.

For future reference, we further introduce the mass-based number density $N_\rho(l, \mathbf{x}, t)$,

$$N_\rho(l, \mathbf{x}, t) = \frac{N(l, \mathbf{x}, t)}{\rho(\mathbf{x}, t)}. \tag{7}$$

The LES-PBE-PDF modelling framework is based on an evolution equation for the LES-filtered one-point, one-time probability density function (*pdf*) associated with a single realization of the instantaneous reactive scalar fields $\mathbf{Y}(\mathbf{x},t)$ and the mass-based number density $N_\rho(\cdot,\mathbf{x},t)$ [52],

$$f(\mathbf{y},n(\cdot);\mathbf{x},t)=\overline{\delta\left(\mathbf{y}-\mathbf{Y}(\mathbf{x},t)\right)\delta\left(n(\cdot)-N_\rho(\cdot,\mathbf{x},t)\right)}. \tag{8}$$

Physically, f is an LES-specific measure of the likelihood for the fluid composition $\mathbf{Y}(\mathbf{x},t)$ at $(\mathbf{x},t)$ to coincide with the sample space vector $\mathbf{y}$ and for the mass-based particle size distribution $N_\rho(\cdot,\mathbf{x},t)$ to coincide with the sample function $n(\cdot)$ on $[l_l,L]$. The overbar in Eq. (8) indicates the LES-operator; recall that the LES-operator is linear and that application of the LES-operator and space/time differentiation commute [47]. Compared with the standard joint scalar LES-PDF formulation, the *pdf* $f(\mathbf{y},n(\cdot);\mathbf{x},t)$ in Eq. (8) is augmented by a functional dependence on the sample space size distribution $n(\cdot)$. If the Gâteaux variation $\partial_{v(\cdot)}f(\mathbf{y},n(\cdot);\mathbf{x},t)$ of $f(\mathbf{y},n(\cdot);\mathbf{x},t)$ in the direction of $v(\cdot)$ exists for all test distributions $v(\cdot)$ and is linear in $v(\cdot)$, then we have the unique Gâteau differential $\partial f(\mathbf{y},n(\cdot);\mathbf{x},t)/\partial n(\cdot)$ with

$$\partial_{v(\cdot)}f(\mathbf{y},n(\cdot);\mathbf{x},t)=\left.\frac{d}{d\varepsilon}f(\mathbf{y},n(\cdot)+\varepsilon v(\cdot);\mathbf{x},t)\right|_{\varepsilon=0}\equiv\frac{\partial f(\mathbf{y},n(\cdot);\mathbf{x},t)}{\partial n(\cdot)}v(\cdot)\quad\forall v(\cdot). \tag{9}$$

Here, ε is a scalar coefficient akin to a perturbation parameter and $v(\cdot)$ represents an admissible test particle size distribution that satisfies the Dirichlet boundary conditions on $N_\rho(\cdot,\mathbf{x},t)$ homogeneously.

By standard techniques [23, 35], it is possible to show that the density weighted counterpart

$$\tilde{f}(\mathbf{y},n(\cdot);\mathbf{x},t)=\frac{\hat{\rho}(\mathbf{y})f(\mathbf{y},n(\cdot);\mathbf{x},t)}{\overline{\rho}(\mathbf{x},t)} \tag{10}$$

of $f(\mathbf{y},n(\cdot);\mathbf{x},t)$ evolves according to [52]

$$\begin{aligned}\overline{\rho}\frac{\partial\tilde{f}}{\partial t}+\sum_{j=1}^{3}\overline{\rho}\tilde{u}_j\frac{\partial\tilde{f}}{\partial x_j}=&\sum_{j=1}^{3}\frac{\partial}{\partial x_j}\left(\overline{\rho}\left(\tilde{u}_j-\overline{(u_j|\,\mathbf{y},n(\cdot))}\right)\tilde{f}\right)-\overline{\rho}\sum_{i=1}^{n_s}\frac{\partial}{\partial y_i}\left(\dot{\omega}_i(\mathbf{y},\hat{\rho}(\mathbf{y})n(\cdot))\tilde{f}+\mathcal{M}_i\tilde{f}\right)\\&-\overline{\rho}\frac{\partial}{\partial n(\cdot)}\left(\frac{\dot{s}(\cdot,\mathbf{y},\hat{\rho}(\mathbf{y})n(\cdot))}{\hat{\rho}(\mathbf{y})}-\frac{\partial G(\cdot,\mathbf{y})n(\cdot)}{\partial l}\right)\tilde{f}\end{aligned} \tag{11}$$

with

$$\mathcal{M}_i\tilde{f}(\mathbf{y},n(\cdot);\mathbf{x},t)=-\frac{1}{\hat{\rho}(\mathbf{y})}\sum_{j=1}^{3}\overline{\left(\frac{\partial J_{ij}(\mathbf{x},t)}{\partial x_j}\middle|\,\mathbf{y},n(\cdot)\right)}\tilde{f}(\mathbf{y},n(\cdot);\mathbf{x},t),\quad i=1,\ldots,n_s. \tag{12}$$

Here, a superimposed tilde indicates Favre filtering [10] and the vertical bars refer to conditional filtering based on the events $\mathbf{Y}(\mathbf{x},t)=\mathbf{y}$ and $N_\rho(\cdot,\mathbf{x},t)=n(\cdot)$. Physically, the first term on the left hand side of Eq. (11) represents local accumulation of likelihood, while the second term indicates transport by the Favre-filtered velocity field. The first term on the right hand side, moreover, encompasses effects due to turbulent transport in physical space. The final two terms cause transport in the joint $(\mathbf{y},n(\cdot))$-sample space on account of chemical reactions, radiation, gas phase molecular mixing and particle formation.

For the closure of the turbulent transport and molecular mixing terms in Eq. (12), we adopt the gradient diffusion hypothesis as well as an extension of the interaction by exchange with the mean (IEM) micromixing model [24], respectively,

$$\overline{\rho}\left(\tilde{u}_j-\overline{(u_j|\,\mathbf{y},n(\cdot))}\right)\tilde{f}=\overline{\rho}\Gamma(\mathbf{x},t)\frac{\partial\tilde{f}}{\partial x_j},\quad j=1,\ldots,3, \tag{13}$$

$$\mathcal{M}_i\tilde{f}=\underbrace{\left(\kappa(\mathbf{x},t)\left(\tilde{Y}_i-y_i\right)+\frac{1}{\overline{\rho}}\sum_{j=1}^{3}\frac{\partial}{\partial x_j}\left(\overline{\rho}\tilde{D}\frac{\partial\tilde{Y}_i}{\partial x_j}\right)\right)}_{\equiv m_i(\mathbf{x},t,\mathbf{y})}\tilde{f},\quad i=1,\ldots,n_s. \tag{14}$$

The closure schemes in Eqs. (13) and (14) rely on two additional kinetic variables, a scaled eddy viscosity $\Gamma(\mathbf{x},t)$ and a micromixing frequency $\kappa(\mathbf{x},t)$ [52]. Introducing Eqs. (13) and (14) into Eq. (11) yields the

following modelled joint scalar-number density *pdf* transport equation,

$$\begin{aligned}\overline{\rho}\frac{\partial \tilde{f}}{\partial t}+\sum_{j=1}^{3}\overline{\rho}\tilde{u}_j\frac{\partial \tilde{f}}{\partial x_j}=\sum_{j=1}^{3}\frac{\partial}{\partial x_j}\left(\overline{\rho}\Gamma\frac{\partial \tilde{f}}{\partial x_j}\right)-\overline{\rho}\sum_{i=1}^{n_s}\frac{\partial}{\partial y_i}\left(\dot{\omega}_i(\mathbf{y},\hat{\rho}(\mathbf{y})n(\cdot))+m_i(\mathbf{x},t,\mathbf{y})\right)\tilde{f}\\ -\overline{\rho}\frac{\partial}{\partial n(\cdot)}\left(\frac{\dot{s}(\cdot,\mathbf{y},\hat{\rho}(\mathbf{y})n(\cdot))}{\hat{\rho}(\mathbf{y})}-\frac{\partial G(\cdot,\mathbf{y})n(\cdot)}{\partial l}\right)\tilde{f}.\end{aligned} \tag{15}$$

Eq. (15) forms the basis of the LES-PBE-PDF framework. Since, in many practical applications, the soot volume fraction remains low (on the order of $\sim 1\,\mathrm{ppb}$ [20, 39] up to $\sim 10\,\mathrm{ppm}$ [19]) and since soot particles behave non-inertially, the governing flow field is computed from the LES-filtered continuity and momentum equations associated with the gas phase only [12, Section 5.3]; in particular, any mass or momentum source/sink terms related to the presence of a disperse particulate phase are omitted. In order to model the residual stress tensor in the LES-filtered momentum equation, we adopt the standard Smagorinsky model [10, Section 4.2.2] with length scale $C_S\Delta$ and $C_S = 0.1$, where Δ is evaluated as the cubic root of the local cell volume. Although the governing flow is thus computed for a single gaseous phase, the formation of soot particles may indirectly affect the ambient flow via modification of the gas phase composition and mixture density (Eq. (6)), for example, due to scavenging of gas phase species or radiation.

In the following three sections, our emphasis lies on the numerical solution of Eq. (15) in a Eulerian fashion.

3 Method of Eulerian stochastic fields

Instead of resolving the *pdf* $\tilde{f}(\mathbf{y}, n(\cdot); \mathbf{x}, t)$ in Eq. (15) directly, many common solution schemes for high-dimensional convection-diffusion-reaction equations involve the construction of a stochastic process whose associated transition *pdf* coincides with (or can be related to [53]) $\tilde{f}(\mathbf{y}, n(\cdot); \mathbf{x}, t)$ in Ω for all times $t \geq 0$ and are based on the approximation of statistics via Monte Carlo estimates. The method of Eulerian stochastic fields [46, 55] is based on a stochastic process $\boldsymbol{\theta}(t; l, \mathbf{x}) = (\theta_1(t;\mathbf{x}), \ldots, \theta_{n_s}(t;\mathbf{x}), \theta_{N_\rho}(t; l, \mathbf{x}))$ which is driven by Brownian motion $\mathbf{W}(t)$ in time and smoothly parameterized by the spatial coordinates [52],[2]

$$\begin{aligned}\overline{\rho}\frac{\partial \theta_i}{\partial t}+\sum_{j=1}^{3}\overline{\rho}\tilde{u}_j\frac{\partial \theta_i}{\partial x_j}=\sum_{j=1}^{3}\frac{\partial}{\partial x_j}\left(\overline{\rho}\Gamma\frac{\partial \theta_i}{\partial x_j}\right)-\overline{\rho}\sqrt{2\Gamma}\sum_{j=1}^{3}\frac{\partial \theta_i}{\partial x_j}\dot{W}_j(t)\\ +\overline{\rho}\left(\dot{\omega}_i(\boldsymbol{\theta})+m_i(\mathbf{x},t,\boldsymbol{\theta})\right),\quad i=1,\ldots,n_s,\end{aligned} \tag{16}$$

$$\begin{aligned}\overline{\rho}\frac{\partial \theta_{N_\rho}}{\partial t}+\sum_{j=1}^{3}\overline{\rho}\tilde{u}_j\frac{\partial \theta_{N_\rho}}{\partial x_j}+\overline{\rho}\frac{\partial G(l,\boldsymbol{\theta})\theta_{N_\rho}}{\partial l}=\sum_{j=1}^{3}\frac{\partial}{\partial x_j}\left(\overline{\rho}\Gamma\frac{\partial \theta_{N_\rho}}{\partial x_j}\right)-\overline{\rho}\sqrt{2\Gamma}\sum_{j=1}^{3}\frac{\partial \theta_{N_\rho}}{\partial x_j}\dot{W}_j(t)\\ +\frac{\overline{\rho}}{\hat{\rho}(\boldsymbol{\theta})}\dot{s}(l,\boldsymbol{\theta}).\end{aligned} \tag{17}$$

Since the transition *pdf* $h(\mathbf{y}, n(\cdot), t; \mathbf{x})$ associated with $\boldsymbol{\theta}(t;\cdot,\mathbf{x})$ evolves according to Eq. (15) [52, Appendix A], statistics of $\tilde{f}(\mathbf{y}, n(\cdot); \mathbf{x}, t)$ can be approximated by Monte Carlo estimates based on sample realizations of $\boldsymbol{\theta}(t;\cdot,\mathbf{x})$. For example, the Favre-filtered value of an observable $\Phi(\mathbf{Y}(\mathbf{x},t), N_\rho(\cdot,\mathbf{x},t))$ may be estimated from

$$\begin{aligned}\tilde{\Phi}(\mathbf{Y}(\mathbf{x},t),N_\rho(\cdot,\mathbf{x},t))&=\frac{\overline{\hat{\rho}(\mathbf{Y}(\mathbf{x},t))\Phi(\mathbf{Y}(\mathbf{x},t),N_\rho(\cdot,\mathbf{x},t))}}{\overline{\rho}(\mathbf{x},t)}=\int\Phi(\mathbf{y},n(\cdot))\tilde{f}(\mathbf{y},n(\cdot);\mathbf{x},t)d\mathbf{y}dn(\cdot)\\ &\approx\frac{1}{n_f}\sum_{i=1}^{n_f}\Phi(\boldsymbol{\theta}^{(i)}(t;\cdot,\mathbf{x}))\equiv\left\langle\Phi(\boldsymbol{\theta}(t;\cdot,\mathbf{x}))\right\rangle_{n_f},\end{aligned} \tag{18}$$

where the superscript $^{(i)}$, $i = 1, \ldots, n_f$, refers to one out of n_f realizations of $\boldsymbol{\theta}(t;\cdot,\mathbf{x})$ and the angled brackets $\langle\cdot\rangle_{n_f}$ indicate a Monte Carlo estimate based on n_f stochastic fields of an expectation with respect

[2] With a slight abuse of notation, we write, for brevity, $G(l,\boldsymbol{\theta})$ and $\dot{s}(l,\boldsymbol{\theta})$ instead of $G(l,\theta_1(t;\mathbf{x}),\ldots,\theta_{n_s}(t;\mathbf{x}))$ and $\dot{s}(l,\theta_1(t;\mathbf{x}),\ldots,\theta_{n_s}(t;\mathbf{x}),\hat{\rho}(\boldsymbol{\theta})\theta_{N_\rho}(t;\cdot,\mathbf{x}))$, respectively, and similarly for $\hat{\rho}(\boldsymbol{\theta})$, $\dot{\boldsymbol{\omega}}(\boldsymbol{\theta})$ and $\mathbf{m}(\mathbf{x},t,\boldsymbol{\theta})$.

to $h(\mathbf{y}, n(\cdot), t; \mathbf{x})$. One consequence of Eq. (18) is that the LES-filtered density can be estimated from the stochastic fields according to [12, Section 4.1]

$$\overline{\rho}(\mathbf{x},t) = \left(\widetilde{\hat{\rho}(\mathbf{Y}(\mathbf{x},t))^{-1}}\right)^{-1} = \left(\int \frac{1}{\hat{\rho}(\mathbf{y})}\tilde{f}(\mathbf{y}, n(\cdot); \mathbf{x}, t)\, d\mathbf{y}dn(\cdot)\right)^{-1} \approx \left(\frac{1}{n_f}\sum_{i=1}^{n_f}\frac{1}{\hat{\rho}(\boldsymbol{\theta}^{(i)})}\right)^{-1}. \tag{19}$$

In engineering applications, the moments $M_k(\mathbf{x}, t)$ of the particle size distribution $N(\cdot, \mathbf{x}, t)$ often play an important role; $M_0(\mathbf{x}, t)$, for example, corresponds to the total number density of particles and $M_1(\mathbf{x}, t)$, $M_3(\mathbf{x}, t)$ represent the mean particle size and a measure of particle volume fraction, respectively. In view of Eqs. (6), (7), (10) and (18), we obtain the following Monte Carlo estimate for the LES-filtered moments (per unit of volume in Ω)

$$\begin{aligned}\overline{M}_k(\mathbf{x},t) &= \overline{\int_{l_l}^{L} l^k N(l,\mathbf{x},t)\, dl} = \overline{\rho}(\mathbf{x},t)\int_{l_l}^{L} l^k \int n(\cdot)\tilde{f}(\mathbf{y}, n(\cdot); \mathbf{x}, t)\, d\mathbf{y}dn(\cdot)\Big|_l\, dl \\ &\approx \frac{\overline{\rho}(\mathbf{x},t)}{n_f}\sum_{i=1}^{n_f}\int_{l_l}^{L} l^k \theta_{N_\rho}^{(i)}(t; l, \mathbf{x})\, dl,\end{aligned} \tag{20}$$

where the long vertical bar indicates "evaluation at".

Except for the dependence of the reaction source/sink terms on $\theta_{N_\rho}(t; \cdot, \mathbf{x})$, Eq. (16) coincides with the stochastic field formulation of the joint scalar *pdf* transport equation [15, 16]; in the presence of a polydisperse particulate phase and for a formulation based on the joint scalar-number density *pdf* transport equation, Eq. (16) is augmented by the stochastic field process for the mass-based particle number density in Eq. (17). Since the numerical solution of Eq. (16) has been addressed previously [38], we confine the attention to Eq. (17) in the following section and detail, in continuous terms, the application of a coordinate transformation on particle size space as well as the derivation of a fractional steps scheme. Conceptually, this provides the basis for the adaptive l-grid discretization scheme proposed by Sewerin and Rigopoulos [50].

Redefining $\theta_N(t; l, \mathbf{x}) \equiv \overline{\rho}(\mathbf{x}, t)\theta_{N_\rho}(t; l, \mathbf{x})$ and taking into account the LES-filtered continuity equation reveals that Eq. (17) is very similar to the original PBE in Eq. (3) apart from the driving Brownian motion,

$$\begin{aligned}\frac{\partial\theta_N}{\partial t} + \sum_{j=1}^{3}\frac{\partial\tilde{v}_j\theta_N}{\partial x_j} + \frac{\partial G(l,\boldsymbol{\theta})\theta_N}{\partial l} &= \sum_{j=1}^{3}\frac{\partial}{\partial x_j}\left(\Gamma\frac{\partial\theta_N}{\partial x_j}\right) - \sqrt{2\Gamma}\sum_{j=1}^{3}\left(\frac{\partial\theta_N}{\partial x_j} - \frac{\theta_N}{\overline{\rho}}\frac{\partial\overline{\rho}}{\partial x_j}\right)\dot{W}_j(t) \\ &\quad + \frac{\overline{\rho}}{\hat{\rho}(\boldsymbol{\theta})}\dot{s}(l,\boldsymbol{\theta})\end{aligned} \tag{21}$$

with

$$\tilde{v}_j = \tilde{u}_j + \frac{\Gamma}{\overline{\rho}}\frac{\partial\overline{\rho}}{\partial x_j}, \quad j = 1, \ldots, 3. \tag{22}$$

4 An adaptive l-resolution formulation and fractional time stepping

In view of an adaptive l-grid discretization [50], we introduce a time and space dependent coordinate transformation $\bar{l}(\tau, \mathbf{x}, t)$ on particle size space $[l_l, L]$ with inverse $\bar{\tau}(l, \mathbf{x}, t)$ and Jacobian $w(\tau, \mathbf{x}, t) = \partial\bar{l}(\tau, \mathbf{x}, t)/\partial\tau$ and define a transformed stochastic number density $\phi_N(t; \tau, \mathbf{x})$ by[3]

$$\theta_N(t; l, \mathbf{x}) \equiv \phi_N(t; \bar{\tau}(l, \mathbf{x}, t), \mathbf{x}). \tag{23}$$

The main idea for time-explicit resolution adaptivity in l-space is to change the coordinate transformation $\bar{l}(\tau, \mathbf{x}, t)$ commensurate with past solutions for $\langle\theta_N(t; l, \mathbf{x})\rangle_{n_f}$. This leads to a time marching scheme in which the coordinate transformation $\bar{l}(\tau, \mathbf{x}, \cdot)$ over the upcoming time step $t \in [t_n, t_{n+1}]$ is constructed explicitly based on the current coordinate transformation $\bar{l}(\tau, \mathbf{x}, t_n)$ and the current number density

[3] For clarity, we employ the short overbar $\bar{\cdot}$ to distinguish between the coordinate transformation ($\bar{l}$ and $\bar{\tau}$) and particular values of physical or transformed size (l and τ). The long overbar $\overline{\cdot}$, on the other hand, indicates the LES-operator.

$\langle\theta_N(t_n;l,\mathbf{x})\rangle_{n_f}$ (or, by Eq. (23), $\langle\phi_N(t_n;\tau,\mathbf{x})\rangle_{n_f}$). By introducing Eq. (23) into Eq. (21), applying the chain rule and evaluating at $\bar{l}(\tau,\mathbf{x},t)$, we obtain the following stochastic field equation for the transformed number density $\phi_N(t;\tau,\mathbf{x})$,

$$\begin{aligned}\frac{\partial\phi_N}{\partial t}+\sum_{j=1}^{3}\frac{\partial\tilde{v}_j\phi_N}{\partial x_j}+\phi_N\left.\frac{\partial G(l,\boldsymbol{\theta})}{\partial l}\right|_{\bar{l}}+\frac{1}{w}\frac{\partial\phi_N}{\partial\tau}\left(G|_{\bar{l}}-g\right)=\sum_{j=1}^{3}\frac{\partial}{\partial x_j}\left(\Gamma\frac{\partial\phi_N}{\partial x_j}\right)+\frac{\overline{\rho}}{\hat{\rho}(\boldsymbol{\theta})}\dot{s}(\bar{l},\boldsymbol{\theta},\phi_N)\\ -\sqrt{2\Gamma}\sum_{j=1}^{3}\left(\frac{\partial\phi_N}{\partial x_j}-\frac{\phi_N}{\overline{\rho}}\frac{\partial\overline{\rho}}{\partial x_j}\right)\dot{W}_j(t)+\frac{\Gamma}{w^2}\frac{\partial}{\partial\tau}\left(\sum_{j=1}^{3}\left(\frac{\partial\bar{l}}{\partial x_j}\right)^2\frac{\partial\phi_N}{\partial\tau}\right)\\ -\frac{2}{w}\sum_{j=1}^{3}\frac{\partial}{\partial x_j}\left(\Gamma\frac{\partial\bar{l}}{\partial x_j}\frac{\partial\phi_N}{\partial\tau}\right)\end{aligned}\tag{24}$$

with

$$g(\tau,\mathbf{x},t)=\frac{\partial\bar{l}}{\partial t}+\sum_{j=1}^{3}\left(\tilde{v}_j+\frac{\partial\Gamma}{\partial x_j}+\sqrt{2\Gamma}\dot{W}_j(t)\right)\frac{\partial\bar{l}}{\partial x_j}-\Gamma b(\tau,\mathbf{x},t),\tag{25}$$

$$b(\tau,\mathbf{x},t)=\frac{1}{w^2}\frac{\partial^2\bar{l}}{\partial\tau^2}\sum_{j=1}^{3}\left(\frac{\partial\bar{l}}{\partial x_j}\right)^2-\sum_{j=1}^{3}\frac{\partial^2\bar{l}}{\partial x_j^2}.\tag{26}$$

Note that, apart from the contribution of the Wiener term and density variability, Eqs. (25) and (26) slightly differ from Eqs. (21) and (16) of Sewerin and Rigopoulos [50] since the mixed derivatives term on the far right of Eq. (24) has been formulated in a different way than in Eq. (15) of Sewerin and Rigopoulos [50].

If Eqs. (16) and (24) are decomposed using a fractional time stepping method, then dedicated solution schemes can be applied, targeting, in turn, the physical characteristics of convection/diffusion, reaction and particle formation. In particular, we obtain for a first order accurate fractional steps method [35, Section 6.3] and on taking $\phi_N(t;\tau,\mathbf{x})\equiv\overline{\rho}(\mathbf{x},t)\phi_{N_\rho}(t;\tau,\mathbf{x})$ (with the aid of Eq. (22) and the LES-filtered continuity equation) the following joint scalar-transformed number density convection-diffusion step

$$\overline{\rho}\frac{\partial\theta_i}{\partial t}+\sum_{j=1}^{3}\overline{\rho}\tilde{u}_j\frac{\partial\theta_i}{\partial x_j}=\sum_{j=1}^{3}\frac{\partial}{\partial x_j}\left(\overline{\rho}\Gamma\frac{\partial\theta_i}{\partial x_j}\right)-\overline{\rho}\sqrt{2\Gamma}\sum_{j=1}^{3}\frac{\partial\theta_i}{\partial x_j}\dot{W}_j(t),\quad i=1,\ldots,n_s,\tag{27}$$

$$\overline{\rho}\frac{\partial\phi_{N_\rho}}{\partial t}+\sum_{j=1}^{3}\overline{\rho}\tilde{u}_j\frac{\partial\phi_{N_\rho}}{\partial x_j}=\sum_{j=1}^{3}\frac{\partial}{\partial x_j}\left(\overline{\rho}\Gamma\frac{\partial\phi_{N_\rho}}{\partial x_j}\right)-\overline{\rho}\sqrt{2\Gamma}\sum_{j=1}^{3}\frac{\partial\phi_{N_\rho}}{\partial x_j}\dot{W}_j(t).\tag{28}$$

The micromixing and chemical reaction fractional steps, moreover, read

$$\frac{\partial\theta_i}{\partial t}=m_i(\mathbf{x},t,\boldsymbol{\theta}),\quad i=1,\ldots,n_s,\tag{29}$$

$$\frac{\partial\theta_i}{\partial t}=\dot{\omega}_i(\boldsymbol{\theta}),\quad i=1,\ldots,n_s.\tag{30}$$

For the PBE fractional step we found it advantageous to retain the volume-based description using $\phi_N(t;\tau,\mathbf{x})$. Slightly reformulating the terms involving l- and τ-derivatives in Eq. (24) yields

$$\begin{aligned}\frac{\partial\phi_N}{\partial t}+\frac{1}{w}\frac{\partial}{\partial\tau}\left(\phi_N\left(G|_{\bar{l}}-g\right)\right)=-\frac{\phi_N}{w}\frac{\partial g}{\partial\tau}+\frac{\Gamma}{w^2}\frac{\partial}{\partial\tau}\left(\sum_{j=1}^{3}\left(\frac{\partial\bar{l}}{\partial x_j}\right)^2\frac{\partial\phi_N}{\partial\tau}\right)\\ -\frac{2}{w}\sum_{j=1}^{3}\frac{\partial}{\partial x_j}\left(\Gamma\frac{\partial\bar{l}}{\partial x_j}\frac{\partial\phi_N}{\partial\tau}\right)+\frac{\overline{\rho}}{\hat{\rho}(\boldsymbol{\theta})}\dot{s}(\bar{l},\boldsymbol{\theta},\phi_N).\end{aligned}\tag{31}$$

While Eqs. (27), (29) and (30) are well-established, Eqs. (28) and (31) are particular to the stochastic field reformulation of the joint scalar-number density *pdf* transport equation in the presence of resolution adaptivity along the particle size coordinate. Eq. (28) can be solved in the same way as Eq. (27); by

contrast, a direct discretization of Eq. (31) is more intricate owing to the occurrence of temporal and spatial derivatives of the coordinate transformation $\bar{l}(\tau, \mathbf{x}, t)$. In order to enhance the accessibility of our numerical solution scheme, we present the requisite details for a finite volume discretization in l- and $\mathbf{x}$-space leading to a complete semi-discrete formulation of Eq. (31) in the following section. For clarity, the attention is confined to the spatially one-dimensional counterpart of Eq. (31), but we indicate extensions to three spatial dimensions.

5 Finite volume discretization of the PBE fractional step

In one spatial dimension, the PBE fractional step in Eq. (31) simplifies to

$$\begin{aligned}\frac{\partial \phi_N}{\partial t} + \frac{1}{w}\frac{\partial}{\partial \tau}\left(\phi_N \left(G|_{\bar{l}} - g\right)\right) = -\frac{\phi_N}{w}\frac{\partial g}{\partial \tau} + \frac{\Gamma}{w^2}\frac{\partial}{\partial \tau}\left(\left(\frac{\partial \bar{l}}{\partial x}\right)^2 \frac{\partial \phi_N}{\partial \tau}\right) \\ - \frac{2}{w}\frac{\partial}{\partial x}\left(\Gamma \frac{\partial \bar{l}}{\partial x}\frac{\partial \phi_N}{\partial \tau}\right) + \frac{\overline{\rho}}{\hat{\rho}(\boldsymbol{\theta})}\dot{s}(\bar{l}, \boldsymbol{\theta}, \phi_N).\end{aligned} \tag{32}$$

In view of a finite volume discretization in $(\tau, x) \in [l_l, L] \times \Omega$, $\Omega = [x_l, x_r]$, we introduce a uniform grid of cell face values in τ-space,

$$\tau_{i+\frac{1}{2}} = l_l + i\Delta\tau, \quad \Delta\tau = \frac{L - l_l}{n_p}, \quad i = 0, \ldots, n_p, \tag{33}$$

along with a possibly non-uniform grid on Ω,

$$x_l = x_{\frac{1}{2}} < x_{\frac{3}{2}} < \ldots < x_{j-\frac{1}{2}} < x_{j+\frac{1}{2}} < \ldots < x_{n_c-\frac{1}{2}} < x_{n_c+\frac{1}{2}} = x_r, \quad j = 1, \ldots, n_c, \tag{34}$$

where integer indices are used to indicate cell midpoints,

$$\tau_i = \frac{\tau_{i-\frac{1}{2}} + \tau_{i+\frac{1}{2}}}{2}, \quad i = 1, \ldots, n_p, \tag{35}$$

$$x_j = \frac{x_{j-\frac{1}{2}} + x_{j+\frac{1}{2}}}{2}, \quad j = 1, \ldots, n_c, \tag{36}$$

and x_l and x_r represent, respectively, the left and right boundary values of Ω. For brevity, the width of a spatial finite volume cell is denoted by $\Delta x_j = x_{j+\frac{1}{2}} - x_{j-\frac{1}{2}}$.

Within the scope of a finite volume approach, the (τ, x)-discrete representation of $\phi_N(t; \tau, x)$ is based on cell averages $\{\Phi_{i,j}(t); i = 1, \ldots, n_p, j = 1, \ldots, n_c\}$ with

$$\Phi_{i,j}(t) \equiv \langle \Phi_i(t; x) \rangle_{\Omega_j} \equiv \frac{1}{\Delta x_j}\int_{x_{j-\frac{1}{2}}}^{x_{j+\frac{1}{2}}} \Phi_i(t; x)\, dx \tag{37}$$

and

$$\Phi_i(t; x) = \frac{1}{\Delta\tau}\int_{\tau_{i-\frac{1}{2}}}^{\tau_{i+\frac{1}{2}}} \phi_N(t; \tau, x)\, d\tau. \tag{38}$$

In Eq. (37), we have introduced subscripted angled brackets $\langle\cdot\rangle_{\Omega_j}$ to indicate spatial averages on $\Omega_j = [x_{j-\frac{1}{2}}, x_{j+\frac{1}{2}}]$ as this notation aids our description of an extension of the semi-discrete formulation to three spatial dimensions. A key assumption we frequently invoke in the following is that $\phi_N(t; \tau, x)$ takes on the value $\Phi_i(t; x)$ on $[\tau_{i-\frac{1}{2}}, \tau_{i+\frac{1}{2}}]$ and, similarly, that $\Phi_i(t; x)$ equals $\Phi_{i,j}(t)$ identically on Ω_j. Furthermore, the coordinate transformation $\bar{l}(\tau, x, t)$ is constructed progressively according to the algorithm proposed by Sewerin and Rigopoulos [50, Section 5]; its main properties which we also refer to below are that $\bar{l}(\tau, x, t)$ varies piecewise linearly on the τ-grid in Eq. (33) such that

$$w(\tau, x, t) = \frac{\partial \bar{l}(\tau, x, t)}{\partial \tau} = w_i(x, t) \quad \text{on } [\tau_{i-\frac{1}{2}}, \tau_{i+\frac{1}{2}}], \quad i = 1, \ldots, n_p, \tag{39}$$

and that $\bar{l}(\tau, x, \cdot)$ changes linearly in time over a time step $[t_n, t_{n+1}]$. This second property relates to the time marching progression; here, the future coordinate transformation $\bar{l}(\tau, x_j, t_{n+1})$ at a cell midpoint

x_j is constructed from the current coordinate transformation $\bar{l}(\tau, x_j, t_n)$ at x_j and the semi-discrete representation of the cell-averaged transformed particle size distribution $\{\langle \Phi_{i,j}(t_n)\rangle_{n_f}\}_{i=1}^{n_p}$ on Ω_j.

For a consistent evaluation of the fluxes that originate from the mixed-derivatives term (see Eqs. (63) and (64) below), we require the spatial derivatives of $\bar{l}(\tau, x, t)$ to be continuous at the spatial cell faces. Since, in spatially discrete terms, the coordinate transformation associated with the semi-discrete transformed particle size distribution $\{\langle \Phi_{i,j}(t)\rangle_{n_f}\}_{i=1}^{n_p}$ in cell Ω_j is prescribed at the cell midpoint x_j, the continuity of $\partial \bar{l}(\tau, x, t)/\partial x$ at $x_{j\pm\frac{1}{2}}$ can be guaranteed by letting $\bar{l}(\tau, x, t)$ vary quadratically in x on Ω_j,

$$\bar{l}(\tau, x(\xi), t) = \bar{l}(\tau, x_j, t) + \left(\left.\frac{\partial \bar{l}}{\partial x}\right|_{x_{j-\frac{1}{2}}} + \left.\frac{\partial \bar{l}}{\partial x}\right|_{x_{j+\frac{1}{2}}} \right) \frac{\Delta x_j}{4}\xi + \left(\left.\frac{\partial \bar{l}}{\partial x}\right|_{x_{j+\frac{1}{2}}} - \left.\frac{\partial \bar{l}}{\partial x}\right|_{x_{j-\frac{1}{2}}} \right) \frac{\Delta x_j}{8}\xi^2, \tag{40}$$

where $x(\xi) = x_{j-\frac{1}{2}} + (1+\xi)\Delta x_j/2$ with $\xi \in [-1, 1]$ refers to a reparameterization of Ω_j and the spatial derivatives of $\bar{l}(\tau, x, t)$ at the cell faces are expressed in terms of the coordinate transformations at adjacent cell midpoints,

$$\left.\frac{\partial \bar{l}}{\partial x}\right|_{x_{j+\frac{1}{2}}} = \frac{\bar{l}(\tau, x_{j+1}, t) - \bar{l}(\tau, x_j, t)}{x_{j+1} - x_j}, \quad j = 0, \ldots, n_c. \tag{41}$$

5.1 Convection, diffusion and reaction in transformed particle size space

In order to slightly simplify the exposition, we defer the treatment of the Wiener and mixed-derivatives terms in Eq. (32) to the two subsequent sections and first address the semi-discrete formulation of Eq. (32) in the absence of these terms. Averaging Eq. (32) over $[\tau_{i-\frac{1}{2}}, \tau_{i+\frac{1}{2}}]$ and taking into account Eq. (39) (while omitting the Wiener and mixed-derivatives terms) leads to

$$\begin{aligned} \frac{\partial \Phi_i}{\partial t} + \frac{1}{w_i \Delta\tau}\left[\phi_N\left(G|_{\bar{l}} - g'\right)\right]_{\tau_{i-\frac{1}{2}}}^{\tau_{i+\frac{1}{2}}} &= -\frac{\Phi_i}{w_i \Delta\tau}\left(g'|_{\tau_{i+\frac{1}{2}}} - g'|_{\tau_{i-\frac{1}{2}}} \right) \\ &+ \frac{\Gamma}{w_i^2 \Delta\tau^2}\left(\left(\frac{\partial \bar{l}}{\partial x}\right)\Big|_{\tau_{i+\frac{1}{2}}}^2 (\Phi_{i+1} - \Phi_i) - \left(\frac{\partial \bar{l}}{\partial x}\right)\Big|_{\tau_{i-\frac{1}{2}}}^2 (\Phi_i - \Phi_{i-1}) \right) \\ &+ \frac{\overline{\rho}}{\hat{\rho}(\boldsymbol{\theta})\Delta\tau}\int_{\tau_{i-\frac{1}{2}}}^{\tau_{i+\frac{1}{2}}} \dot{s}(\bar{l}, \boldsymbol{\theta}, \phi_N)\, d\tau \end{aligned} \tag{42}$$

with

$$g'(\tau, x, t) = \frac{\partial \bar{l}}{\partial t} + \left(\tilde{v} + \frac{\partial \Gamma}{\partial x}\right)\frac{\partial \bar{l}}{\partial x} + \Gamma \frac{\partial^2 \bar{l}}{\partial x^2}. \tag{43}$$

On the right hand side of Eq. (42), the cell face values of $\partial \phi_N(t; \tau, x)/\partial\tau$ were approximated by linear interpolation between the cell averaged values at adjacent cell midpoints. For the convection term, a high resolution formulation is commonly applied [40, 41]; here, the cell face values $\phi_N(t; \tau, x)$ are represented as a linear combination of the cell averages in the neighbouring cells, for example [21],

$$\phi_N|_{\tau_{i+\frac{1}{2}}} = \Phi_{u(\tau_{i+\frac{1}{2}})} + \frac{r(\tau_{i+\frac{1}{2}}, x, t)}{2}\left(\Phi_{u(\tau_{i+\frac{1}{2}})} - \Phi_{uu(\tau_{i+\frac{1}{2}})}\right), \tag{44}$$

where $u(\tau_{i+\frac{1}{2}})$ and $uu(\tau_{i+\frac{1}{2}})$ are the indices of the two cells upstream of cell face $\tau_{i+\frac{1}{2}}$ and $r(\tau_{i+\frac{1}{2}}, x, t) \in [0, 2]$ denotes a flux limiter.

Multiplying Eq. (42) by $w_i(x, t)$ and spatially averaging over Ω_j, we arrive at the following semi-discrete formulation

$$\begin{aligned} \langle w_i\rangle_{\Omega_j}\frac{d\Phi_{i,j}}{dt} + \frac{1}{\Delta\tau}\left[\phi_j\left(G(\langle \bar{l}\rangle_{\Omega_j}, \boldsymbol{\theta}_j) - \langle g'\rangle_{\Omega_j}\right)\right]_{\tau_{i-\frac{1}{2}}}^{\tau_{i+\frac{1}{2}}} &= -\frac{\Phi_{i,j}}{\Delta\tau}\left[\langle g'\rangle_{\Omega_j}\right]_{\tau_{i-\frac{1}{2}}}^{\tau_{i+\frac{1}{2}}} \\ &+ \frac{1}{\Delta\tau^2}\left(\left\langle \frac{\Gamma}{w_i}\left(\frac{\partial \bar{l}}{\partial x}\right)\Big|_{\tau_{i+\frac{1}{2}}}^2 \right\rangle_{\Omega_j} (\Phi_{i+1,j} - \Phi_{i,j}) - \left\langle \frac{\Gamma}{w_i}\left(\frac{\partial \bar{l}}{\partial x}\right)\Big|_{\tau_{i-\frac{1}{2}}}^2 \right\rangle_{\Omega_j} (\Phi_{i,j} - \Phi_{i-1,j}) \right) \\ &+ \frac{\overline{\rho}_j}{\hat{\rho}(\boldsymbol{\theta}_j)\Delta\tau}\langle w_i\rangle_{\Omega_j}\int_{\tau_{i-\frac{1}{2}}}^{\tau_{i+\frac{1}{2}}} \dot{s}(\langle \bar{l}\rangle_{\Omega_j}, \boldsymbol{\theta}_j, \phi_j)\, d\tau \end{aligned} \tag{45}$$

with $\phi_j(t;\tau) = \langle \phi_N(t;\tau,x)\rangle_{\Omega_j}$, $\boldsymbol{\theta}_j(t) = \langle \boldsymbol{\theta}(t;x)\rangle_{\Omega_j}$, $\overline{\rho}_j(t) = \langle \overline{\rho}(x,t)\rangle_{\Omega_j}$ and

$$\left\langle G(\bar{l}(\tau,x,t),\boldsymbol{\theta}(t;x))\right\rangle_{\Omega_j} \approx G(\left\langle \bar{l}(\tau,x,t)\right\rangle_{\Omega_j},\boldsymbol{\theta}_j(t)), \tag{46}$$

$$\left\langle w_i \int_{\tau_{i-\frac{1}{2}}}^{\tau_{i+\frac{1}{2}}} \dot{s}(\bar{l},\boldsymbol{\theta},\phi_N)\,d\tau \right\rangle_{\Omega_j} \approx \langle w_i\rangle_{\Omega_j} \int_{\tau_{i-\frac{1}{2}}}^{\tau_{i+\frac{1}{2}}} \dot{s}(\left\langle \bar{l}\right\rangle_{\Omega_j},\boldsymbol{\theta}_j,\phi_j)\,d\tau. \tag{47}$$

The $\bar{l}$-dependent coefficients in Eq. (45)

$$\langle w_i\rangle_{\Omega_j}, \quad \langle g'\rangle_{\Omega_j}, \quad \left\langle \frac{\Gamma}{w_i}\left(\frac{\partial \bar{l}}{\partial x}\right)^2\right\rangle_{\Omega_j} \approx \frac{1}{\langle w_i\rangle_{\Omega_j}}\left\langle \Gamma\left(\frac{\partial \bar{l}}{\partial x}\right)^2\right\rangle_{\Omega_j} \tag{48}$$

are influenced by the way in which $\bar{l}(\tau,x,t)$ is prescribed to vary in τ, x and t. From Eq. (40), for example, the cell-averaged coordinate transformation $\left\langle \bar{l}(\tau,x,t)\right\rangle_{\Omega_j}$ on Ω_j is obtained as

$$\left\langle \bar{l}(\tau,x,t)\right\rangle_{\Omega_j} = \bar{l}(\tau,x_j,t) + \left(\left.\frac{\partial \bar{l}}{\partial x}\right|_{x_{j+\frac{1}{2}}} - \left.\frac{\partial \bar{l}}{\partial x}\right|_{x_{j-\frac{1}{2}}}\right)\frac{\Delta x_j}{24} \tag{49}$$

and, by Eq. (39), the Jacobian $\langle w(\tau,x,t)\rangle_{\Omega_j}$ reads

$$\langle w_i(x,t)\rangle_{\Omega_j} = \frac{\left\langle \bar{l}(\tau_{i+\frac{1}{2}},x,t)\right\rangle_{\Omega_j} - \left\langle \bar{l}(\tau_{i-\frac{1}{2}},x,t)\right\rangle_{\Omega_j}}{\Delta\tau}, \quad i = 1,\ldots,n_p. \tag{50}$$

Note that $\left\langle \bar{l}(\tau,x,t)\right\rangle_{\Omega_j}$ does not, in general, coincide with the cell midpoint coordinate transformation $\bar{l}(\tau,x_j,t)$ (that is constructed based on $\{\langle \Phi_{i,j}(t)\rangle_{n_f}\}_{i=1}^{n_p}$ in the course of the explicit time marching scheme [50, Section 5]).

By introducing Eq. (40) into Eq. (48)$_2$, assuming $\Gamma(x,t)$ and $\tilde{v}(x,t)$ to change linearly on Ω_j and analytically evaluating the spatial integral, we obtain with the aid of Eq. (43)

$$\begin{aligned}\langle g'\rangle_{\Omega_j} = {} & \left.\dot{\bar{l}}\right|_{x_j} + \frac{\Delta x_j}{24}\left(\left.\frac{\partial \dot{\bar{l}}}{\partial x}\right|_{x_{j+\frac{1}{2}}} - \left.\frac{\partial \dot{\bar{l}}}{\partial x}\right|_{x_{j-\frac{1}{2}}}\right) \\ & + \left(\frac{\tilde{v}|_{x_{j+\frac{1}{2}}} + \tilde{v}|_{x_{j-\frac{1}{2}}}}{2} + \frac{\Gamma|_{x_{j+\frac{1}{2}}} - \Gamma|_{x_{j-\frac{1}{2}}}}{\Delta x_j}\right)\frac{1}{2}\left(\left.\frac{\partial \bar{l}}{\partial x}\right|_{x_{j-\frac{1}{2}}} + \left.\frac{\partial \bar{l}}{\partial x}\right|_{x_{j+\frac{1}{2}}}\right) \\ & + \left(\frac{\tilde{v}|_{x_{j+\frac{1}{2}}} - \tilde{v}|_{x_{j-\frac{1}{2}}}}{6} + \frac{\Gamma|_{x_{j+\frac{1}{2}}} + \Gamma|_{x_{j-\frac{1}{2}}}}{\Delta x_j}\right)\frac{1}{2}\left(\left.\frac{\partial \bar{l}}{\partial x}\right|_{x_{j+\frac{1}{2}}} - \left.\frac{\partial \bar{l}}{\partial x}\right|_{x_{j-\frac{1}{2}}}\right).\end{aligned} \tag{51}$$

To slightly abridge the previous expression, we have used a superimposed dot to indicate partial time differentiation, $\dot{\bar{l}}(\tau,x,t) = \partial \bar{l}(\tau,x,t)/\partial t$. In a similar way, the term in Eq. (48)$_3$ evaluates to

$$\begin{aligned}\left\langle \Gamma\left(\frac{\partial \bar{l}}{\partial x}\right)^2\right\rangle_{\Omega_j} = {} & \left(\frac{\Gamma|_{x_{j-\frac{1}{2}}}}{4} + \frac{\Gamma|_{x_{j+\frac{1}{2}}}}{12}\right)\left.\frac{\partial \bar{l}}{\partial x}\right|^2_{x_{j-\frac{1}{2}}} + \left(\frac{\Gamma|_{x_{j-\frac{1}{2}}}}{12} + \frac{\Gamma|_{x_{j+\frac{1}{2}}}}{4}\right)\left.\frac{\partial \bar{l}}{\partial x}\right|^2_{x_{j+\frac{1}{2}}} \\ & + \frac{\Gamma|_{x_j} + \Gamma|_{x_{j+\frac{1}{2}}}}{6}\left.\frac{\partial \bar{l}}{\partial x}\right|_{x_{j-\frac{1}{2}}}\left.\frac{\partial \bar{l}}{\partial x}\right|_{x_{j+\frac{1}{2}}}.\end{aligned} \tag{52}$$

Since the coordinate transformation $\bar{l}(\tau,x_j,t)$ that is prescribed at the cell midpoints x_j varies linearly over a time interval $[t_n,t_{n+1}]$, the spatial cell averages $\left\langle \bar{l}(\tau,x,t)\right\rangle_{\Omega_j}$ and $\langle g'(\tau,x,t)\rangle_{\Omega_j}$ in Eqs. (49) and (51) also vary linearly in time t, whereas $\left\langle \Gamma(x,t)\left(\partial \bar{l}(\tau,x,t)/\partial x\right)^2\right\rangle_{\Omega_j}$ in Eq. (52) is quadratic in t. Consequently, we may compute the values of these terms at intermediate times $t \in [t_n,t_{n+1}]$ by linear or quadratic interpolation, respectively, based on support values at times t_n, t_{n+1} and, for Eq. (52), $t_{n+\frac{1}{2}} \equiv (t_n + t_{n+1})/2$ (also see rows 7, 8 and 10 in Table 2).

5.2 Wiener term

One term that we had omitted in the derivations of the previous section is the driving Wiener term

$$\frac{\partial \phi_N}{\partial t} = \frac{\sqrt{2\Gamma}\dot{W}(t)}{w}\frac{\partial \bar{l}}{\partial x}\frac{\partial \phi_N}{\partial \tau}. \tag{53}$$

Strictly, Eq. (53) is only formally valid and holds in a time integral sense,

$$\begin{aligned}\phi_N(t_{n+1};\tau,x) &= \phi_N(t_n;\tau,x) + \int_{t_n}^{t_{n+1}} \frac{\sqrt{2\Gamma(x,t)}}{w(\tau,x,t)}\frac{\partial \bar{l}(\tau,x,t)}{\partial x}\frac{\partial \phi_N(t;\tau,x)}{\partial \tau}\,dW(t) \\ &= \phi_N(t_n;\tau,x) + \frac{\sqrt{2\Gamma(x,t_n)}}{w(\tau,x,t_n)}\frac{\partial \bar{l}(\tau,x,t_n)}{\partial x}\frac{\partial \phi_N(t_n;\tau,x)}{\partial \tau}\Delta W_{n+1},\end{aligned} \tag{54}$$

where the stochastic integral on the right hand side is interpreted in Itô's sense [30, Section 3.1] and $\Delta W_{n+1} = W(t_{n+1}) - W(t_n)$ indicates an increment of a continuous-time Wiener process. Within the scope of the Euler-Maruyama integration method [30, Section 5.2], ΔW_{n+1} is approximated by $\xi_{n+1}\sqrt{\Delta t_{n+1}}$, where $\{\xi_n\}_{n=1,2,\ldots}$ are independent Gaussian random variables and $\Delta t_{n+1} = t_{n+1} - t_n$ denotes the current time step. This method is weakly first order accurate in time; the weak order of accuracy is maintained if we adopt the slightly simpler approximation $\Delta W_{n+1} \approx \eta_{n+1}\sqrt{\Delta t_{n+1}}$ based on dichotomic random variables $\{\eta_n\}_{n=1,2,\ldots}$ that take on the values $\{-1, 1\}$ with equal probability [55].

For conciseness, we return to the notation of Eq. (53) for the remaining part of this section, keeping, however, the time integral interpretation and the Euler-Maruyama approximation in mind. Averaging Eq. (53) over a τ-cell $[\tau_{i-\frac{1}{2}}, \tau_{i+\frac{1}{2}}]$ and replacing cell face values $\phi_N(t;\tau_{i+\frac{1}{2}},x)$ by $(\Phi_i(x,t) + \Phi_{i+1}(x,t))/2$ yields

$$w_i\frac{\partial \Phi_i}{\partial t} = \frac{\sqrt{2\Gamma}\dot{W}(t)}{\Delta\tau}\left(\left.\frac{\partial \bar{l}}{\partial x}\right|_{\tau_{i+\frac{1}{2}}}\frac{\Phi_{i+1}-\Phi_i}{2} + \left.\frac{\partial \bar{l}}{\partial x}\right|_{\tau_{i-\frac{1}{2}}}\frac{\Phi_i - \Phi_{i-1}}{2}\right). \tag{55}$$

Upon spatial averaging, we arrive at the semi-discrete representation

$$\langle w_i\rangle_{\Omega_j}\frac{d\Phi_{i,j}}{dt} = \frac{\dot{W}(t)}{\Delta\tau}\left(\left\langle\sqrt{2\Gamma}\left.\frac{\partial \bar{l}}{\partial x}\right|_{\tau_{i+\frac{1}{2}}}\right\rangle_{\Omega_j}\frac{\Phi_{i+1,j}-\Phi_{i,j}}{2} + \left\langle\sqrt{2\Gamma}\left.\frac{\partial \bar{l}}{\partial x}\right|_{\tau_{i-\frac{1}{2}}}\right\rangle_{\Omega_j}\frac{\Phi_{i,j}-\Phi_{i-1,j}}{2}\right), \tag{56}$$

where, by Eq. (40) and taking $\Gamma_j(t) = \langle\Gamma(x,t)\rangle_{\Omega_j}$,

$$\left\langle\sqrt{2\Gamma}\left.\frac{\partial \bar{l}}{\partial x}\right|_{\tau_{i+\frac{1}{2}}}\right\rangle_{\Omega_j} \approx \sqrt{2\Gamma_j(t)}\left\langle\left.\frac{\partial \bar{l}}{\partial x}\right|_{\tau_{i+\frac{1}{2}}}\right\rangle_{\Omega_j} = \frac{\sqrt{2\Gamma_j(t)}}{2}\left(\left.\frac{\partial \bar{l}}{\partial x}\right|_{x_{j-\frac{1}{2}}} + \left.\frac{\partial \bar{l}}{\partial x}\right|_{x_{j+\frac{1}{2}}}\right)\Bigg|_{\tau_{i+\frac{1}{2}}}. \tag{57}$$

In order to avoid spurious negative values of the transformed stochastic number densities $\Phi_{i,j}(t_{n+1})$, the right hand side (rhs) of Eq. (56) is limited by

$$\text{Rhs of Eq. (56)} \longleftarrow \max\left(\text{Rhs of Eq. (56)}, -\langle w_i\rangle_{\Omega_j}\frac{\Phi_{i,j}(t_n)}{\Delta t_{n+1}} - \text{Rhs of Eq. (63) below}\right), \tag{58}$$

where the left pointing arrow indicates a substitution operation and the flux terms on the right hand side of Eq. (63) are modified according to Eq. (66) below.

5.3 Mixed-derivatives term

In this section, we consider separately the finite volume discretization of the mixed-derivatives term on the right hand side of Eq. (32),

$$\frac{\partial \phi_N}{\partial t} = -\frac{2}{w}\frac{\partial}{\partial x}\left(\Gamma\frac{\partial \bar{l}}{\partial x}\frac{\partial \phi_N}{\partial \tau}\right), \tag{59}$$

or, equivalently,

$$w\frac{\partial \phi_N}{\partial t} = -2\frac{\partial}{\partial x}\left(\Gamma\frac{\partial}{\partial \tau}\left(\phi_N\frac{\partial \bar{l}}{\partial x}\right) - \Gamma\phi_N\frac{\partial^2 \bar{l}}{\partial \tau \partial x}\right). \tag{60}$$

Integrating Eq. (60) over a finite volume cell in τ-space, $[\tau_{i-\frac{1}{2}}, \tau_{i+\frac{1}{2}}]$, and dividing by the uniform cell width $\Delta\tau$ yields

$$w_i \frac{\partial \Phi_i}{\partial t} = -\frac{\partial}{\partial x}\left(\frac{\Gamma}{\Delta\tau}\left((\Phi_{i+1}-\Phi_i)\left.\frac{\partial \bar{l}}{\partial x}\right|_{\tau_{i+\frac{1}{2}}} + (\Phi_i - \Phi_{i-1})\left.\frac{\partial \bar{l}}{\partial x}\right|_{\tau_{i-\frac{1}{2}}}\right)\right), \tag{61}$$

where cell face values of $\phi_N(t;\tau,x)$ were approximated by linear interpolation of the cell averages at adjacent cell mid-points and we have also made use of the fact that the coordinate transformation $\bar{l}(\tau,x,t)$ varies piece-wise linearly in τ, whence

$$\frac{\partial^2 \bar{l}}{\partial\tau\partial x} = \frac{1}{\Delta\tau}\left(\left.\frac{\partial \bar{l}}{\partial x}\right|_{\tau_{i+\frac{1}{2}}} - \left.\frac{\partial \bar{l}}{\partial x}\right|_{\tau_{i-\frac{1}{2}}}\right) \quad \text{for} \quad \tau \in [\tau_{i-\frac{1}{2}}, \tau_{i+\frac{1}{2}}]. \tag{62}$$

If Eq. (61) is averaged in turn over a spatial finite volume cell Ω_j, then we obtain the semi-discrete representation

$$\langle w_i \rangle_{\Omega_j} \frac{d\Phi_{i,j}}{dt} = \frac{1}{\Delta\tau \Delta x_j}\left(h^{(\mathrm{mix})}_{i,j+\frac{1}{2}} - h^{(\mathrm{mix})}_{i,j-\frac{1}{2}}\right), \tag{63}$$

where the Jacobian $\langle w_i(x,t)\rangle_{\Omega_j}$ is evaluated according to Eq. (50) and $h^{(\mathrm{mix})}_{i,j\pm\frac{1}{2}}$ correspond to the fluxes (in $[1/\mathrm{m}^2 - \mathrm{s}]$) entering cell $[\tau_{i-\frac{1}{2}}, \tau_{i+\frac{1}{2}}] \times \Omega_j$ across the left and right boundaries, respectively,

$$h^{(\mathrm{mix})}_{i,j+\frac{1}{2}} = -\left.\Gamma\right|_{x_{j+\frac{1}{2}}}\left(\left.\frac{\partial \bar{l}}{\partial x}\right|_{\tau_{i+\frac{1}{2}}}(\Phi_{i+1}-\Phi_i) + \left.\frac{\partial \bar{l}}{\partial x}\right|_{\tau_{i-\frac{1}{2}}}(\Phi_i - \Phi_{i-1})\right)\Bigg|_{x_{j+\frac{1}{2}}}. \tag{64}$$

The spatial cell face values $\Phi_i(t; x_{j+\frac{1}{2}})$ in Eq. (64) can be computed in terms of the cell averages $\Phi_{i,j}(t)$ of adjacent cells by standard linear interpolation. Note that the stencil on the right hand side of Eq. (63) encompasses cells that are adjacent to cell (i,j) both in the τ- and x-directions and, thus, results in a coupling of the discrete transformed particle size distributions $\{\Phi_{i,j}(t)\}_{i=1}^{n_p}$ in all spatial grid cells. In order to circumvent this coupling and restore spatial independence of grid cells in the PBE fractional step, we apply a forward Euler approximation in time to Eq. (63), evaluating the cell averages $\Phi_{i,j}(t)$ on its right hand side at the current time instant. Concomitantly, the spatial derivatives of the coordinate transformation $\bar{l}(\tau,x,t)$ are also evaluated at the current point in time.

In order for the discrete particle size distributions to remain non-negative, the cumulative flux out of cell (i,j) on the right hand side of Eq. (63) is limited in magnitude by the maximum admissible outflux $-\langle w_i\rangle_{\Omega_j}\Phi_{i,j}(t_n)/\Delta t_{n+1}$ over the time interval $[t_n, t_{n+1}]$. In practice, we found the following *ad hoc* limiting procedure to work reliably. Those cell face fluxes $h^{(\mathrm{mix})}_{i,\star}$ which contribute a sink term on the right hand side of Eq. (63),

$$0 \geq \frac{1}{\Delta\tau\Delta x_j}\left(\min\left(0, h^{(\mathrm{mix})}_{i,j+\frac{1}{2}}\right) - \max\left(0, h^{(\mathrm{mix})}_{i,j-\frac{1}{2}}\right)\right), \tag{65}$$

are scaled by a factor α if the right hand side of Eq. (65) is negative

$$h^{(\mathrm{mix})}_{i,\star} \longleftarrow \alpha h^{(\mathrm{mix})}_{i,\star} \quad \text{with} \quad \alpha = \min\left(1, -\frac{\langle w_i\rangle_{\Omega_j}}{\Delta t_{n+1}}\frac{\Phi_{i,j}(t_n)}{\text{Rhs of Eq. (65)}}\right). \tag{66}$$

Here, $\star$ refers to an index set that encompasses the indices of those cell face fluxes which are directed out of cell Ω_j; for example, $\star = \{j+\frac{1}{2}\}$ if $h^{(\mathrm{mix})}_{i,j\pm\frac{1}{2}} < 0$ and $\star = \{j\pm\frac{1}{2}\}$ if $h^{(\mathrm{mix})}_{i,j+\frac{1}{2}} < 0$ and $h^{(\mathrm{mix})}_{i,j-\frac{1}{2}} > 0$.

5.4 Interim summary of the semi-discrete formulation and generalization to three spatial dimensions

In summary, the (τ,x)-discretization approach detailed above results in the following semi-discrete formulation in terms of the cell-averaged transformed stochastic number density $\Phi_{i,j}(t)$, $t \in [t_n, t_{n+1}]$,

$$\langle w_i\rangle_{\Omega_j}\frac{d\Phi_{i,j}}{dt} = \text{Rhs of Eq. (45)} + \text{Rhs of Eq. (56)} + \text{Rhs of Eq. (63)} \tag{67}$$

subject to the limiting operations detailed in Eqs. (58), (65) and (66). Owing to the Euler-Maruyama and explicit Euler integration schemes of the two preceding sections, the final two terms in Eq. (67) are evaluated at the current time t_n, constituting constant source terms on $[t_n, t_{n+1}]$, and may, hence, be evaluated in an initialization phase before a time integration subroutine is called on Eq. (67).

Since the evaluation of cell-averaged LES-filtered moments $\langle \overline{M}_k(x,t) \rangle_{\Omega_j}$ would evolve spatial cell averages of powers of the coordinate transformation $\langle \bar{l}(\tau, x, t)^k \rangle_{\Omega_j}$, we report, for simplicity and efficiency, semi-discrete LES-filtered moments at the cell centers (as in References [51, 52]); by Eq. (20),

$$\overline{M}_k(x_j,t) = \frac{1}{n_f} \sum_{m=1}^{n_f} \sum_{i=1}^{n_p} \Phi_{i,j}^{(m)}(t) \left[\frac{\bar{l}(\tau, x_j, t)^{k+1}}{k+1} \right]_{\tau_{i-\frac{1}{2}}}^{\tau_{i+\frac{1}{2}}}. \tag{68}$$

As above, the parenthesized superscript index $^{(m)}$ refers to the mth realization of the semi-discrete transformed stochastic number densities $\{\Phi_{i,j}(t); i = 1, \ldots, n_p, j = 1, \ldots, n_c\}$.

For a structured rectilinear grid, the semi-discrete formulation we presented so far for a single spatial dimension ($x = x_1$) can be generalized to three spatial dimensions (x, y, z) by summing the flux contributions on the right hand side of Eq. (67) for all spatial coordinate directions [29]. For example, the semi-discrete counterpart of the transformed PBE only involving the mixed derivatives term in Eq. (63) may be evaluated according to

$$\begin{aligned} \langle w_i \rangle_{\Omega_{jkl}} \frac{d\Phi_{i,jkl}}{dt} = \frac{1}{\Delta\tau} \Bigg[& \frac{1}{\Delta x_j} \left(h_{i,j+\frac{1}{2}}^{(\mathrm{mix})} - h_{i,j-\frac{1}{2}}^{(\mathrm{mix})} \right) + \frac{1}{\Delta y_k} \left(h_{i,k+\frac{1}{2}}^{(\mathrm{mix})} - h_{i,k-\frac{1}{2}}^{(\mathrm{mix})} \right) \\ & + \frac{1}{\Delta z_l} \left(h_{i,l+\frac{1}{2}}^{(\mathrm{mix})} - h_{i,l-\frac{1}{2}}^{(\mathrm{mix})} \right) \Bigg], \end{aligned} \tag{69}$$

where (j,k,l) are triple indices of the spatial grid cell Ω_{jkl} with midpoint $\mathbf{x}_{jkl}$ and a single subscript j, k or l indicates the direction of spatial derivatives ($x_1 = x$, $x_2 = y$ or $x_3 = z$) in the flux computations of Eqs. (64) and (66).

In an extension of Eq. (40) to three spatial dimensions, we prescribe the coordinate transformation $\bar{l}(\tau, \mathbf{x}, t)$ to vary quadratically in each coordinate direction over Ω_{jkl},

$$\begin{aligned} \bar{l}(\tau, \mathbf{x}(\boldsymbol{\xi}), t) = \bar{l}(\tau, \mathbf{x}_{jkl}, t) & + \left(\left.\frac{\partial \bar{l}}{\partial x}\right|_{x_{j-\frac{1}{2}}} + \left.\frac{\partial \bar{l}}{\partial x}\right|_{x_{j+\frac{1}{2}}} \right) \frac{\Delta x_j}{4} \xi + \left(\left.\frac{\partial \bar{l}}{\partial x}\right|_{x_{j+\frac{1}{2}}} - \left.\frac{\partial \bar{l}}{\partial x}\right|_{x_{j-\frac{1}{2}}} \right) \frac{\Delta x_j}{8} \xi^2 \\ & + \left(\left.\frac{\partial \bar{l}}{\partial y}\right|_{y_{k-\frac{1}{2}}} + \left.\frac{\partial \bar{l}}{\partial y}\right|_{y_{k+\frac{1}{2}}} \right) \frac{\Delta y_k}{4} \eta + \left(\left.\frac{\partial \bar{l}}{\partial y}\right|_{y_{k+\frac{1}{2}}} - \left.\frac{\partial \bar{l}}{\partial y}\right|_{y_{k-\frac{1}{2}}} \right) \frac{\Delta y_k}{8} \eta^2 \\ & + \left(\left.\frac{\partial \bar{l}}{\partial z}\right|_{z_{l-\frac{1}{2}}} + \left.\frac{\partial \bar{l}}{\partial z}\right|_{z_{l+\frac{1}{2}}} \right) \frac{\Delta z_l}{4} \zeta + \left(\left.\frac{\partial \bar{l}}{\partial z}\right|_{z_{l+\frac{1}{2}}} - \left.\frac{\partial \bar{l}}{\partial z}\right|_{z_{l-\frac{1}{2}}} \right) \frac{\Delta z_l}{8} \zeta^2, \end{aligned} \tag{70}$$

where $\boldsymbol{\xi} = (\xi, \eta, \zeta) \in [-1, 1]^2$ are reparameterization coordinates with $x(\xi) = x_{j-\frac{1}{2}} + (1+\xi)\Delta x_j/2$ and similarly for $y(\eta)$ and $z(\zeta)$. The spatial derivatives of $\bar{l}(\tau, \mathbf{x}, t)$ at the cell faces in Eq. (70) are evaluated in a similar way as in Eq. (41). Note that although the coordinate transformation $\bar{l}(\tau, \mathbf{x}, t)$ reconstructed on Ω_{jkl} in Eq. (70) is discontinuous across cell faces in general, its spatial derivatives are always continuous across the cell faces in the coordinate direction along which the derivates are taken and, hence, the fluxes on the right hand side of Eq. (69) are consistent across adjacent cells. Schematically, the spatial variation of $\bar{l}(\tau, \mathbf{x}, t)$ over four finite volume cells of a two-dimensional rectilinear grid is illustrated in Figure 1 for a fixed value of τ and a given time instant t.

Spatially averaging Eq. (70) on Ω_{jkl} yields the following cell-averaged coordinate transformation

$$\begin{aligned} \left\langle \bar{l}(\tau, \mathbf{x}, t) \right\rangle_{\Omega_{jkl}} = \bar{l}(\tau, \mathbf{x}_{jkl}, t) & + \left(\left.\frac{\partial \bar{l}}{\partial x}\right|_{x_{j+\frac{1}{2}}} - \left.\frac{\partial \bar{l}}{\partial x}\right|_{x_{j-\frac{1}{2}}} \right) \frac{\Delta x_j}{24} + \left(\left.\frac{\partial \bar{l}}{\partial y}\right|_{y_{k+\frac{1}{2}}} - \left.\frac{\partial \bar{l}}{\partial y}\right|_{y_{k-\frac{1}{2}}} \right) \frac{\Delta y_k}{24} \\ & + \left(\left.\frac{\partial \bar{l}}{\partial z}\right|_{z_{l+\frac{1}{2}}} - \left.\frac{\partial \bar{l}}{\partial z}\right|_{z_{l-\frac{1}{2}}} \right) \frac{\Delta z_l}{24}. \end{aligned} \tag{71}$$

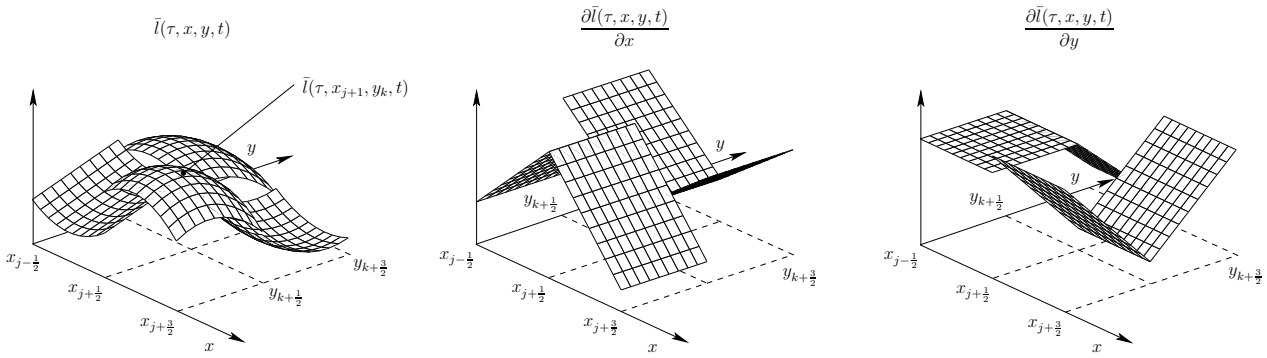

Figure 1: Illustration of the change in two spatial coordinates of the coordinate transformation $\bar{l}(\tau,\cdot,t)$ (left panel) reconstructed from cell midpoint coordinate transformations $\bar{l}(\tau,\mathbf{x}_{jk},t)$ and of its spatial derivatives $\partial\bar{l}(\tau,\cdot,t)/\partial x$, $\partial\bar{l}(\tau,\cdot,t)/\partial y$ (center and right panels) for $\mathbf{x}=(x,y)$ at a specific time instant t and a given value for $\tau\in[l_l,L]$.

By a direct extension of Eqs. (51) and (52), moreover, we obtain on account of Eq. (70) and supposing that, in each term, $\tilde{\mathbf{v}}(\mathbf{x},t)$ and $\Gamma(\mathbf{x},t)$ vary linearly only in the coordinate direction along which the spatial derivative of $\bar{l}(\tau,\mathbf{x},t)$ is taken

$$\langle g'(\tau,\mathbf{x},t)\rangle_{\Omega_{jkl}} = \dot{\bar{l}}\Big|_{\mathbf{x}_{jkl}} + \sum_{i=1}^{3}\left(\text{Terms } 2-4 \text{ on rhs of Eq. (51) for } x=x_i\right), \tag{72}$$

$$\left\langle \Gamma\sum_{i=1}^{3}\left(\frac{\partial\bar{l}}{\partial x_i}\right)^2\right\rangle_{\Omega_{jkl}} = \sum_{i=1}^{3}\left(\text{Rhs of Eq. (52) for } x=x_i\right). \tag{73}$$

Similarly, the coefficients $\dot{W}(t)\left\langle\sqrt{2\Gamma}\,\partial\bar{l}/\partial x\big|_{\tau_{i+\frac{1}{2}}}\right\rangle_{\Omega_j}$, $i=0,\ldots,n_p$, on the right hand side of Eq. (56) are replaced by

$$\sum_{i=1}^{3}\dot{W}_i(t)\left(\text{Rhs of Eq. (57) for } x=x_i\right). \tag{74}$$

6 Dynamic load balancing

Both the reaction and PBE fractional steps can be solved independently for each spatial grid cell. Such problems are sometimes referred to as embarrassingly parallel as no synchronization between results obtained for different grid points is needed. Commonly, implementations of reactive flow solvers are parallelized with the aid of a domain decomposition technique, whereby every computing process owns a particular part of the physical flow domain and boundary values are communicated using halo cell layers. In such an implementation, the workload associated with the solution of the reaction and PBE fractional steps on each process can differ depending on the number of cells in each subdomain whose composition is amenable to reaction or on the stiffness of the chemical reaction and PBE ODE (ordinary differential equation) systems, for instance.

The expected workload on each process may be estimated either using heuristic techniques or based on physical insight. In our current implementation, the reaction fractional step is limited to those cells whose temperature exceeds a minimum temperature of $T=800\,\mathrm{K}$; concomitantly, we take the number of reacting cells within a process' subdomain as an estimate for its expected workload. Implicit here is the assumption that all reacting ODE systems require approximately the same amount of work or runtime for integration. While this may not hold true in general, we obtain some justification from the use of a first order backward Euler ODE integrator without step size refinement. The kinetic rate expressions are obtained from the Chemkin library [17] and hard-coded. For efficiency, all temperature-dependent coefficients are evaluated only once at the beginning of the reaction fractional step and maintained over a time step; at the end of the reaction step, the temperature is then updated based on the final composition

(Eq. (5)). Lastly, we mention that, in order to avoid evaluating the Jacobian repeatedly, the backward Euler non-linear system is solved using a modified Newton-Raphson scheme.

The PBE fractional step, on the other hand, is executed on all physical cells since changes in the transformed stochastic number density may also result on account of spatial/temporal variability of the coordinate transformation on particle size space even if the kinetic rates for particle formation vanish (Eq. (31)). In this case, we estimate the expected workload on a process in terms of previous runtime measurements on the integration of the ODE systems associated with all grid cells in the process' subdomain. For the very first time step, the workload on each process is assumed to be identical. In order to temporally integrate the PBE fractional step, we apply the explicit 5th order accurate Runge-Kutta method DOPRI5 of Hairer et al. [11] with error control. Despite the simplicity of our approaches for estimating the workloads on each process for the reaction and PBE fractional steps, we find that they perform very well at reducing significantly the load imbalance (see Figure 4 below).

In a similar way as for the PBE fractional step, the prospective workload associated with the reaction fractional step may also be estimated based on past runtime measurements if the composition in a cell continues to be flammable. Although this does not have a bearing on our current approach, where the workload associated with every chemical ODE system is similar, it may be attractive for more general time integrators involving error control and step size refinement. However, considering a backward Euler solver with step size refinement, we observed that, contrary to the PBE step, past runtimes are not always indicative or representative of the current stiffness of a chemical reaction ODE system. One possible reason for this is that the remaining fractional steps significantly affect the local gas composition either due to convective/diffusive transport, molecular mixing or scavenging of gas phase species and radicals by particle formation and depletion. In the case of soot formation, radiation can also exert a large influence on the local gas enthalpy. The soot particle size distribution, by contrast, evolves on much larger time scales and is not amenable to molecular diffusion; typically nucleation and oxidation are reported as the fastest physical processes, while surface growth proceeds slower [3].

In a methodology for dynamic load balancing, the cumulative workload is redistributed among all processes in such a way that every process is assigned an approximately equal share. While, in some applications, the exchange of work among processes is restricted by the connectivity of the processes' physical subdomains [54], we do not encounter such restrictions here owing to the embarrassingly parallel nature of the reaction and PBE fractional steps. Redistributing work relies on a bilateral communication pattern among those processes whose workloads exceed or fall below the average workload across all processes (plus/minus a preset tolerance). Figure 2 lists the algorithm we currently use on each process in order to determine the recipients and corresponding workload sizes of parcels that a process sends (if its initial workload exceeds the average workload) or the senders and equivalent workloads of parcels a process receives (if its initial workload is smaller than the average workload). Here, a parcel encompasses the input data necessary for the integration of as many ODE systems as amount to the workload that is to be sent or received. On the reverse communication path after integration is complete, the parcels contain the integration output data (along with runtime measurements for the PBE ODE systems). For memory economy, a process employs the same buffer both for sending/receiving input data parcels and receiving back/returning the output data parcels. As reference, the input/output data for an ODE system of the spatially one-dimensional reaction or PBE fractional step that are sent and received via parcels are summarized in Table 2.

The algorithm in Figure 2 proceeds iteratively; in each iteration, the main idea is to match a process whose workload exceeds the average workload with a process whose workload deficit closely matches the surplus workload of the overloaded process. The workload excess and deficit, respectively, are then compensated, partly or completely, the matched sender-receiver pair is stored and the iteration continues to the next remaining overloaded process. The algorithm terminates as soon as all workload excesses have been distributed or do not differ from the average workload by more than a small tolerance.

Schematically, the main steps involved in a dynamic load balancing scheme based on the communication pattern of Figure 2 are illustrated in the flow chart in Figure 3. The boxes shifted to the left hand side indicate the commands issued and tasks performed by receiving processes, while the boxes shifted to the right hand side pertain to sending processes. For both receiving and sending processes, data transfers are non-blocking and overlap with the integration of ODE systems that remain on the current process. If a process receives multiple parcels from different senders, then the ODE systems within a parcel are integrated concurrently with receipt operations for the subsequent parcels and the return delivery of the previous parcels.

For realistic runtime measurements on the dynamic load balancing scheme for the reaction and PBE

In-/output	Reaction fractional step			PBE fractional step		
	Variable	Time	Reference	Variable(s)	Time(s)	Reference(s)
Input	$\boldsymbol{\theta}_j(t)$	t_n		$\boldsymbol{\theta}_j(t)$	t_n	
	$\hat{T}(\boldsymbol{\theta}_j(t))$	t_n	Eq. (5)	$\hat{T}(\boldsymbol{\theta}_j(t))$, $\hat{\rho}(\boldsymbol{\theta}_j(t))$	t_n	Eqs. (5), (6)
				$\Phi_{i,j}(t)$	t_n	Eq. (37)
				Kinetic coefficients	t_n	
				$\langle g'(\tau,x,t)\rangle_{\Omega_j}$	$\{t_n, t_{n+1}\}$	Eq. (51)
				$\left\langle \Gamma\left(\partial\bar{l}(\tau,x,t)/\partial x\right)^2\right\rangle_{\Omega_j}$	$\{t_n, t_{n+\frac{1}{2}}, t_{n+1}\}$	Eq. (52)
				Mixed/Wiener terms	t_n	Rhs of Eqs. (56), (63)
				$\langle \bar{l}(\tau,x,t)\rangle_{\Omega_j}$	$\{t_n, t_{n+1}\}$	Eq. (49)
Output	$\boldsymbol{\theta}_j(t)$	t_{n+1}		$\boldsymbol{\theta}_j(t)$	t_{n+1}	
				$\Phi_{i,j}(t)$	t_{n+1}	
				Integration runtime		Eqs. (45), (56), (63)

Table 2: Summary of the variables per grid cell Ω_j that are sent (rows $3-10$) or returned (rows $11-13$) in a data parcel as part of the dynamic load balancing scheme for the reaction (columns $2-4$) and PBE (columns $5-7$) fractional steps in one spatial dimension. For brevity, we employ the shorthand notation $\boldsymbol{\theta}_j(t) = \langle \boldsymbol{\theta}(x,t)\rangle_{\Omega_j}$. The variables listed in columns 2 and 5 are evaluated at the time instants indicated in columns 3 and 6, respectively. Additionally, the τ-dependent variables in column 4 are computed at the τ-cell faces $\tau_{i+\frac{1}{2}}$ (Eq. (33)) and $i = 0, \ldots, n_p$.

fractional steps, we return to the Delft III test case previously investigated by Sewerin and Rigopoulos [52], implementing two slight amendments. First, molecular mixing of the particle number density is omitted; by consequence, the micromixing fractional step in Eq. (29) does not extend to the stochastic number density. Second, we retrieve inflow profiles for the LES-filtered velocity by applying the digital filter-based procedure of Klein et al. [18] to power law mean profiles based on the nominal jet and co-flow bulk velocities and to velocity covariances estimated from prescribed turbulence intensities. As in the original simulation [52], the spatial grid encompasses $n_c = 672 \times 70 \times 36 = 1,693,440$ cells and transformed particle size space is discretized using $n_p = 30$ finite volume cells.

In order to assess the extent to which our implementation achieves hiding data transfers behind computation/integration, absolute and relative runtime measurements spent on ODE integration are compared with idle and total runtimes in Table 3 for the Delft III test case. Here, relative measurements indicate fractions of the total runtime for the complete reaction or PBE fractional step. The runtime measurements were taken on four nodes (96 MPI processes) of a Cray XC30 Supercomputer (ARCHER UK) and averaged over all MPI processes and 25 consecutive time steps of size $\Delta t = 10^{-6}\,\mathrm{s}$. For the PBE fractional step, we infer from Table 3 that processes remain idle for 1.4 % of the total runtime on average. This observation is very positive; it also carries over to the reaction fractional step, for which idle waiting times account for 1.9 % of the total runtime on average.

Although we reconsider, with slight amendments, the Delft III test case of Sewerin and Rigopoulos [52] here, the time measurements in Table 3 differ from those reported in Table 2 of Sewerin and Rigopoulos [52]. On the one hand, this is due to the fact that the present time measurements were obtained for a slightly smaller time step of $\Delta t = 10^{-6}\,\mathrm{s}$ (compared to $\Delta t = 1.2 \times 10^{-6}\,\mathrm{s}$ in the original reference). On the other hand, Sewerin and Rigopoulos [52] applied the dynamic load balancing scheme only to the reaction fractional step. Furthermore, parcels were received in-order and, for sending processors, the commands for receiving parcels back were only called after *all* parcels had been sent. In the current implementation, we lift these restrictions and also adapt the dynamic load balancing scheme to the PBE fractional step.

We can gain some insight into the efficacy of the dynamic load balancing scheme in either fractional step by examining statistics of the relative load imbalance across all processes. Following Thévenin et al. [54], the relative load imbalance I_i of process i, $i = 1, \ldots, n_{mpi}$, can be defined as the fraction of the average runtime which a process' requires in excess of or less than the average runtime,

$$I_i = \frac{\left|T_i - \bar{T}\right|}{\bar{T}}, \quad \bar{T} = \frac{1}{n_{mpi}} \sum_{i=1}^{n_{mpi}} T_i. \tag{75}$$

Input: $\mathbf{w} = (w_1, \ldots, w_{n_{mpi}})$, $\mathbf{p} = (1, \ldots, n_{mpi})$, id

1. Compute deviation $\mathbf{x} = (x_1, \ldots, x_{n_{mpi}})$ from mean workload $\bar{w}$

$$x_i = w_i - \bar{w}, \quad i = 1, \ldots, n_{mpi}, \quad \bar{w} = \frac{1}{n_{mpi}} \sum_{j=1}^{n_{mpi}} w_j$$

2. Initialize number of parcels to be sent, $n_d = 0$, and to be received, $n_r = 0$, and set a tolerance $\text{tol} = 5\%\bar{w}$
3. Repeatedly loop over all entries of $\mathbf{x}$ with $x_i > 0$

   3.1 If $x_i \leq \text{tol}$, then set $x_i = 0$ and skip to 3.8

   3.2 Determine the value x_j in $\mathbf{x}$ whose negative is closest to x_i

$$x_j = \arg \min_{k=1,\ldots,n_{mpi}} (x_i + \min(0, x_k))$$

   (This indicates that process p_i sends a parcel with corresponding workload $\min(x_i, -x_j)$ to process p_j.)

   3.3 If $x_j \geq 0$, then quit

   3.4 If $p_i = id$, then increment $n_d \leftarrow n_d + 1$ and save $M^{(\text{send})}_{n_d,1} = p_j$, $M^{(\text{send})}_{n_d,2} = \min(x_i, -x_j)$

   3.5 If $p_j = id$, then increment $n_r \leftarrow n_r + 1$ and save $M^{(\text{recv})}_{n_r,1} = p_i$, $M^{(\text{recv})}_{n_r,2} = \min(x_i, -x_j)$

   3.6 Update $x_i \leftarrow \max(0, x_i + x_j)$ and set $x_i = 0$ if $x_i \leq \text{tol}$

   3.7 Update $x_j \leftarrow \min(0, x_i + x_j)$ and set $x_j = 0$ if $x_j \geq -\text{tol}$

   3.8 If $i < n_{mpi}$, then increment $i \leftarrow i+1$ and continue at 3.1; if $\mathbf{x}$ possesses a positive entry and $i > n_{mpi}$, then set $i = 1$ and also continue at 3.1; otherwise quit

Output: n_d, n_r, $\mathbf{M}^{(\text{send})}$, $\mathbf{M}^{(\text{recv})}$

Figure 2: Algorithm for determining the communication schedule of process id, $id \in \{1, \ldots, n_{mpi}\}$, based on the estimated workload $\mathbf{w}$ on all processes with identifiers $\mathbf{p}$. The matrices $\mathbf{M}^{(\text{send})}$ and $\mathbf{M}^{(\text{recv})}$ contain the destinations/sources (first column) and corresponding workloads (second column) for parcels that process id sends or receives, respectively. For example, process id may send a parcel with workload $M^{(\text{send})}_{i,2}$ to process $M^{(\text{send})}_{i,1}$, $i \in \{1, \ldots, n_d\}$. For $w_{id} < \bar{w}$, process id receives a parcel with workload $M^{(\text{recv})}_{j,2}$ from process $M^{(\text{recv})}_{j,1}$, $j \in \{1, \ldots, n_r\}$.

Here, T_i denotes the runtime of a fractional step on process i and $\bar{T}$ refers to the average runtime on all processes. Figure 4(a) depicts the temporal change of the mean load imbalance (lines) across all processes as well as the corresponding standard deviation (shaded areas) for the reaction and PBE fractional steps, while Figure 4(b) shows the maximum relative load imbalance. For reference, we also include measurements of the maximum relative load imbalance that remains if the dynamic load balancing is deactivated. As above, the runtime measurements were performed on the Delft III test case using the same computing configuration and settings. For the PBE fractional step, we observe that the mean relative load imbalance remains below 2.5 % and attains maximum values of 15 % on average. The mean relative load imbalance of the reaction fractional step is slightly smaller, not exceeding 2.0 %, and the maximum imbalance reaches 4 % on average. Figure 4(b) also indicates that the dynamic load balancing scheme is effective at reducing the maximum relative load imbalance from about 190 % and 170 % for the PBE and reaction fractional steps, respectively, by more than an order of magnitude on average.

The strong scaling of a parallel implementation on a multi-processor hardware is often analyzed by comparing runtime measurements on an increasing number of processors for a fixed problem size. In view of a strong scaling analysis for the Delft III test case, Figure 5 depicts the change in runtime per time step (averaged over 100 consecutive time steps) for each fractional step over different numbers of processors or, equivalently, nodes on a Cray XC30 Supercomputer (ARCHER UK). Here, the convection-diffusion, gas phase reaction and PBE fractional steps consume approximately equal shares of the total runtime, while solution of the micromixing fractional step is about one order of magnitude faster. In slight amelioration, we mention that the similarity of absolute runtimes for the former three steps may be coincidental; depending on the intensity of particle nucleation and growth and on the vigorousness of spatial and temporal PBE grid variability, an implicit integration scheme can, possibly, be necessary

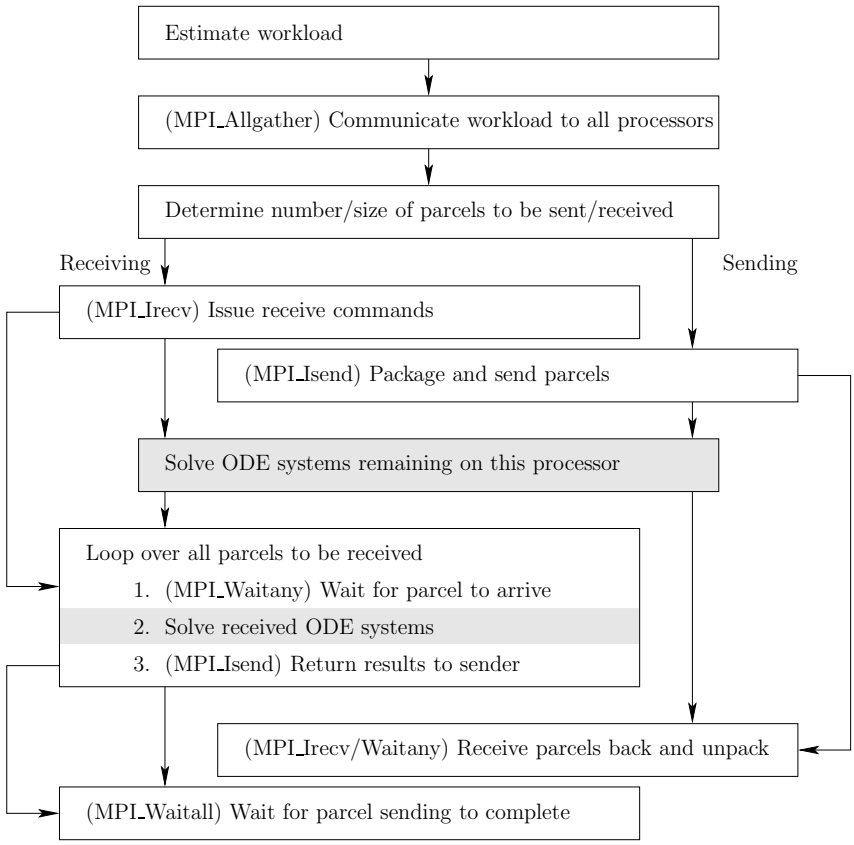

Figure 3: Schematic flow chart illustrating the solution (gray shaded) and communication (MPI-standard commands) steps for processes receiving (left hand side) or sending (right hand side) parcels as part of a dynamic load balancing scheme for the reaction and PBE fractional steps.

Time measurement	Reaction fractional step		PBE fractional step	
	Absolute [s]	Relative [%]	Absolute [s]	Relative [%]
Integration	$4.0 \pm 8.7 \times 10^{-2}$	97.5 ± 1.9	$4.0 \pm 8.4 \times 10^{-2}$	98.6 ± 1.4
Idle	$7.7 \times 10^{-2} \pm 7.8 \times 10^{-2}$	1.9 ± 1.9	$5.5 \times 10^{-2} \pm 5.7 \times 10^{-2}$	1.4 ± 1.4
Total	$4.1 \pm 7.9 \times 10^{-2}$	100	$4.0 \pm 9.8 \times 10^{-2}$	100

Table 3: Runtime measurements (averaged over 25 consecutive time steps and 96 MPI processes on a Cray XC30 Supercomputer, ARCHER UK) of the dynamically load balanced reaction and PBE fractional steps for the Delft III test case (time step $\Delta t = 10^{-6}$ s). Relative values correspond to fractions of the total runtime. Idle times indicate time periods over which processes wait for memory transfers to complete.

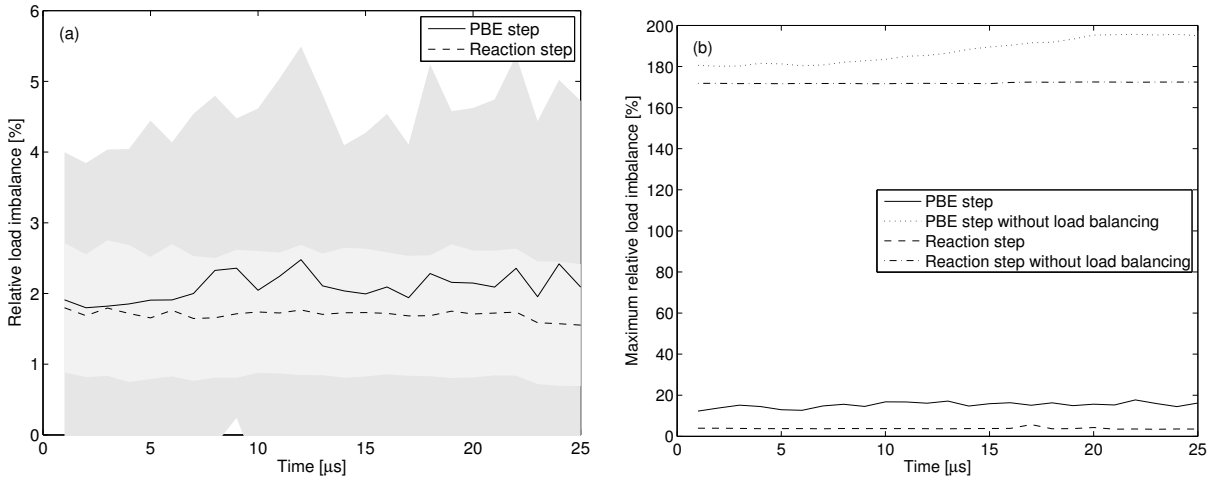

Figure 4: (a) Mean relative load imbalance computed across 96 MPI processes for the reaction and PBE fractional steps of the Delft III test case including a dynamic load balancing scheme. Here, the shaded areas (light/dark gray for the reaction/PBE fractional step) indicate plus/minus one standard deviation. (b) Maximum relative load imbalance across all processes both with and without the dynamic load balancing scheme.

for the solution of the PBE fractional step [51]. Additionally, integration of the chemical kinetics ODE systems has been simplified by evaluating the rate coefficients at the initial temperature and by omitting step size refinement; as a consequence, the workload per ODE system remains approximately constant (safe for variations in the number of modified Newton-Raphson steps for the solution of the backward Euler linear systems) across all reacting grid cells. If we were to employ a more accurate chemical kinetics integrator with error control and step size refinement, then an improved *a priori* estimate of the workload per chemical reaction ODE system would be required; possibly, such an estimate could be based on kinetic criteria, for example, the maximum time scale ratio or, equivalently, a measure of the conditioning of the ODE system. Importantly, however, Figure 5 demonstrates a linear strong scaling (compare with the thick solid line in the top right corner) of the four fractional steps, thus evidencing the effectiveness of our dynamic load balancing scheme.

7 Conclusions

Recently, the LES-PBE-PDF approach has emerged as a viable predictive framework for modelling soot particle size distributions in turbulent hydrocarbon flames. Here, correlations of gas phase composition and soot particle number density are resolved without any approximation on part of the chemical or particle formation kinetics. This is reflected in the modelled evolution equation for the LES-filtered joint scalar-number density *pdf*. In order to estimate LES-related statistics of the composition and particle size distribution, we employed a numerical solution approach based on a statistically equivalent reformulation in terms of Eulerian stochastic fields and invoked an explicit adaptive grid method for discretizing the stochastic field counterpart of the PBE in particle size space.

In this article, we revisited the LES-PBE-PDF framework combined with a Eulerian stochastic field reformulation and provided details on the semi-discrete formulation of the PBE fractional step featuring particle size grid adaptivity. Our emphasis lay on the consistent spatial and temporal evaluation of terms that originate from the adaptive grid discretization in particle size space. Since most of the computational expense persists in the chemical reaction and PBE fractional steps, we further proposed a dynamic load balancing scheme that involves a dedicated bilateral communication pattern for deployment on massively parallel computing systems. The performance of the dynamic load balancing scheme was quantified for a test case of soot formation in the turbulent diffusion flame Delft III; we found the remnant load imbalance in either fractional step to not exceed 2.5 % on average and gave evidence of linear strong scaling on a high performance computer for up to 192 processors.

Apart from our solution approach combining a stochastic field formulation with particle size grid

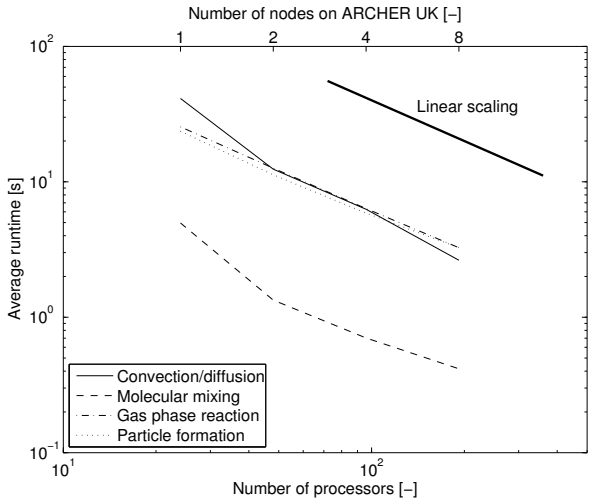

Figure 5: Average runtimes for solving the convection-diffusion (Eqs. (27) and (28)), molecular mixing (Eq. (29)), gas phase reaction (Eq. (30)) and PBE fractional steps (Eq. (31)) on a Cray XC30 Supercomputer (ARCHER UK, 24 processors per node) over the number of processors used for the Delft III test case (time step $\Delta t = 10^{-6}$ s). Here, the problem size remains constant (strong scaling analysis).

adaptivity, an alternative solution strategy based on an MMC/sparse stochastic particle method has been advocated by Neuber et al. [27, 28]. The test cases examined by these authors and in our work [51, 52] corroborate the practical viability of the PBE-PDF extension to LES, but also show that its power is mainly contingent upon the development of efficient numerical solution and parallelization strategies. Potentially, a combination of the MMC/sparse stochastic particle method with an adaptive particle size discretization may enable further runtime reductions without incurring a loss in accuracy – an idea we intend to explore in future times.

Acknowledgements

This work used the ARCHER UK National Supercomputing Service (http://www.archer.ac.uk).

Funding

This work was supported by the UK Consortium on Turbulent Reacting Flows (EP/K026801/1).

References

[1] Akridis, P. (2016). *Coupled CFD-Population Balance Modelling of Soot Formation in Laminar and Turbulent Flames*. PhD thesis, Imperial College London.

[2] Akridis, P. and Rigopoulos, S. (2015). Modelling of soot formation in a turbulent diffusion flame using a comprehensive CFD-PBE model with full chemistry. In *Proceedings of the European Combustion Meeting*, Budapest, Hungary.

[3] Attili, A., Bisetti, F., Mueller, M. E., and Pitsch, H. (2014). Formation, growth, and transport of soot in a three-dimensional turbulent non-premixed jet flame. *Combustion and Flame*, 161(7):1849–1865.

[4] Bisetti, F., Blanquart, G., Mueller, M. E., and Pitsch, H. (2012). On the formation and early evolution of soot in turbulent nonpremixed flames. *Combustion and Flame*, 159(1):317–335.

[5] Di Veroli, G. Y. and Rigopoulos, S. (2009). A study of turbulence-chemistry interaction in reactive precipitation via a population balance-transported PDF method. In Hanjalić, K., Nagano, Y., and

Jakirlić, S., editors, *Proceedings of the sixth International Symposium on Turbulence, Heat and Mass Transfer*, Rome, Italy. Begell House, Inc.

[6] Di Veroli, G. Y. and Rigopoulos, S. (2010). Modeling of turbulent precipitation: A transported population balance-PDF method. *AIChE Journal*, 56(4):878–892.

[7] Di Veroli, G. Y. and Rigopoulos, S. (2011). Modeling of aerosol formation in a turbulent jet with the transported population balance equation-probability density function approach. *Physics of Fluids*, 23(4):043305.

[8] Fox, R. O. (2012). Large-eddy-simulation tools for multiphase flows. *Annual Review of Fluid Mechanics*, 44(1):47–76.

[9] Gao, F. and O'Brien, E. E. (1993). A large-eddy simulation scheme for turbulent reacting flows. *Physics of Fluids A: Fluid Dynamics*, 5:1282–1284.

[10] Garnier, E., Adams, N., and Sagaut, P. (2009). *Large eddy simulation for compressible flows*. Springer Science & Business Media.

[11] Hairer, E., Nørsett, S. P., and Wanner, G. (1993). *Solving Ordinary Differential Equations I: Non-stiff Problems*, volume 8 of *Springer Series in Computational Mathematics*. Springer-Verlag, Berlin, Heidelberg.

[12] Haworth, D. (2010). Progress in probability density function methods for turbulent reacting flows. *Progress in Energy and Combustion Science*, 36(2):168–259.

[13] Hulburt, H. M. and Katz, S. (1964). Some problems in particle technology: A statistical mechanical formulation. *Chemical Engineering Science*, 19(8):555–574.

[14] Jones, W. P. (2002). The joint scalar probability density function method. In Launder, B. E. and Sandham, N., editors, *Closure Strategies for Turbulent and Transitional Flows*, chapter 20, pages 582–625. Cambridge University Press, Cambridge, United Kingdom.

[15] Jones, W. P. and Navarro-Martinez, S. (2007). Large eddy simulation of autoignition with a subgrid probability density function method. *Combustion and Flame*, 150(3):170–187.

[16] Jones, W. P. and Prasad, V. N. (2010). Large eddy simulation of the Sandia flame series (D-F) using the Eulerian stochastic field method. *Combustion and Flame*, 157(9):1621–1636.

[17] Kee, R. J., Rupley, F. M., Meeks, E., and Miller, J. A. (1996). *CHEMKIN-III: A FORTRAN chemical kinetics package for the analysis of gas-phase chemical and plasma kinetics*. Sandia National Laboratories Livermore, CA, USA.

[18] Klein, M., Sadiki, A., and Janicka, J. (2003). A digital filter based generation of inflow data for spatially developing direct numerical or large eddy simulations. *Journal of Computational Physics*, 186(2):652–665.

[19] Köhler, M., Geigle, K. P., Meier, W., Crosland, B. M., Thomson, K. A., and Smallwood, G. J. (2011). Sooting turbulent jet flame: characterization and quantitative soot measurements. *Applied Physics B: Lasers and Optics*, 104(2):409–425.

[20] Koo, H., Hassanaly, M., Raman, V., Mueller, M. E., and Geigle, K. P. (2016). Large-eddy simulation of soot formation in a model gas turbine combustor. *Journal of Engineering for Gas Turbines and Power*, 139(3):031503.

[21] Koren, B. (1993). A robust upwind discretization method for advection, diffusion and source terms. In Vreugdenhil, C. B. and Koren, B., editors, *Numerical Methods for Advection-Diffusion Problems*, volume 45 of *Notes on Numerical Fluid Mechanics and Multidisciplinary Design*, pages 117–138. Vieweg Verlag.

[22] Kronenburg, A., Bilger, R., and Kent, J. H. (2000). Modeling soot formation in turbulent methane-air jet diffusion flames. *Combustion and Flame*, 121(1-2):24–40.

[23] Lundgren, T. S. (1967). Distribution functions in the statistical theory of turbulence. *Physics of Fluids*, 10(5):969–975.

[24] McDermott, R. and Pope, S. B. (2007). A particle formulation for treating differential diffusion in filtered density function methods. *Journal of Computational Physics*, 226(1):947–993.

[25] Mueller, M. E. and Pitsch, H. (2011). Large eddy simulation subfilter modeling of soot-turbulence interactions. *Physics of Fluids*, 23(11):115104.

[26] Mueller, M. E. and Pitsch, H. (2012). LES model for sooting turbulent nonpremixed flames. *Combustion and Flame*, 159(6):2166–2180.

[27] Neuber, G., Garcia, C. E., Kronenburg, A., Williams, B. A. O., Beyrau, F., Stein, O. T., and Cleary, M. J. (2019). Joint experimental and numerical study of silica particulate synthesis in a turbulent reacting jet. *Proceedings of the Combustion Institute*, 37:1213–1220.

[28] Neuber, G., Kronenburg, A., Stein, O. T., and Cleary, M. J. (2017). MMC-LES modelling of droplet nucleation and growth in turbulent jets. *Chemical Engineering Science*, 167:204–218.

[29] Patankar, S. V. (1980). *Numerical Heat Transfer and Fluid Flow*. Hemisphere Publishing Corporation, New York.

[30] Pavliotis, G. A. (2014). *Stochastic Processes and Applications*. Springer, New York.

[31] Pierce, C. D. and Moin, P. (2004). Progress-variable approach for large-eddy simulation of non-premixed turbulent combustion. *Journal of Fluid Mechanics*, 504:73–97.

[32] Pitsch, H. (2006). Large-eddy simulation of turbulent combustion. *Annual Review of Fluid Mechanics*, 38(1):453–482.

[33] Pitsch, H., Riesmeier, E., and Peters, N. (2000). Unsteady flamelet modeling of soot formation in turbulent diffusion flames. *Combustion Science and Technology*, 158(1):389–406.

[34] Pitsch, H. and Steiner, H. (2000). Large-eddy simulation of a turbulent piloted methane/air diffusion flame (Sandia flame D). *Physics of Fluids*, 12(10):2541–2554.

[35] Pope, S. B. (1985). PDF methods for turbulent reactive flows. *Progress in Energy and Combustion Science*, 11(2):119–192.

[36] Pope, S. B. (1991). Computations of turbulent combustion: Progress and challenges. *Symposium (International) on Combustion*, 23(1):591–612.

[37] Pope, S. B. (2010). Self-conditioned fields for large-eddy simulations of turbulent flows. *Journal of Fluid Mechanics*, 652:139–169.

[38] Prasad, V. N. (2011). *Large eddy simulation of partially premixed turbulent combustion*. PhD thesis, Imperial College London.

[39] Qamar, N. H., Alwahabi, Z. T., Chan, Q. N., Nathan, G. J., Roekaerts, D., and King, K. D. (2009). Soot volume fraction in a piloted turbulent jet non-premixed flame of natural gas. *Combustion and Flame*, 156(7):1339–1347.

[40] Qamar, S., Ashfaq, A., Warnecke, G., Angelov, I., Elsner, M. P., and Seidel-Morgenstern, A. (2007). Adaptive high-resolution schemes for multidimensional population balances in crystallization processes. *Computers and Chemical Engineering*, 31(10):1296–1311.

[41] Qamar, S., Elsner, M. P., Angelov, I. A., Warnecke, G., and Seidel-Morgenstern, A. (2006). A comparative study of high resolution schemes for solving population balances in crystallization. *Computers and Chemical Engineering*, 30(6-7):1119–1131.

[42] Raman, V. and Fox, R. O. (2016). Modeling of fine-particle formation in turbulent flames. *Annual Review of Fluid Mechanics*, 48:159–190.

[43] Rigopoulos, S. (2007). PDF method for population balance in turbulent reactive flow. *Chemical Engineering Science*, 62(23):6865–6878.

[44] Rigopoulos, S. (2010). Population balance modelling of polydispersed particles in reactive flows. *Progress in Energy and Combustion Science*, 36(4):412–443.

[45] Rodrigues, P., Franzelli, B., Vicquelin, R., Gicquel, O., and Darabiha, N. (2018). Coupling an LES approach and a soot sectional model for the study of sooting turbulent non-premixed flames. *Combustion and Flame*, 190:477–499.

[46] Sabel'nikov, V. and Soulard, O. (2005). Rapidly decorrelating velocity-field model as a tool for solving one-point Fokker-Planck equations for probability density functions of turbulent reactive scalars. *Physical Review E*, 72(1):016301.

[47] Sagaut, P. (2006). *Large Eddy Simulation for Incompressible Flows: An Introduction*. Springer, Berlin, 3rd edition.

[48] Schiener, M. A. and Lindstedt, R. P. (2018). Joint-scalar transported PDF modelling of soot in a turbulent non-premixed natural gas flame. *Combustion Theory and Modelling*, 22(6):1134–1175.

[49] Schiener, M. A. and Lindstedt, R. P. (2019). Transported probability density function based modelling of soot particle size distributions in non-premixed turbulent jet flames. *Proceedings of the Combustion Institute*, 37:1049–1056.

[50] Sewerin, F. and Rigopoulos, S. (2017a). An explicit adaptive grid approach for the numerical solution of the population balance equation. *Chemical Engineering Science*, 168:250–270.

[51] Sewerin, F. and Rigopoulos, S. (2017b). An LES-PBE-PDF approach for modeling particle formation in turbulent reacting flows. *Physics of Fluids*, 29(10):105105.

[52] Sewerin, F. and Rigopoulos, S. (2018). An LES-PBE-PDF approach for predicting the soot particle size distribution in turbulent flames. *Combustion and Flame*, 189:62–76.

[53] Soulard, O. and Sabelnikov, V. A. (2006). Eulerian Monte Carlo method for the joint velocity and mass-fraction probability density function in turbulent reactive gas flows. *Combustion, Explosion and Shock Waves*, 42(6):753–762.

[54] Thévenin, D., Behrendt, F., Maas, U., Przywara, B., and Warnatz, J. (1996). Development of a parallel direct simulation code to investigate reactive flows. *Computers & Fluids*, 25(5):485–496.

[55] Valiño, L. (1998). A field Monte Carlo formulation for calculating the probability density function of a single scalar in a turbulent flow. *Flow, Turbulence and Combustion*, 60(2):157–172.

[56] Vo, S., Kronenburg, A., Stein, O. T., and Cleary, M. J. (2017). Multiple mapping conditioning for silica nanoparticle nucleation in turbulent flows. *Proceedings of the Combustion Institute*, 36(1):1089–1097.